Lawrence Berkeley National Laboratory
Recent Work

Title
IDENTIFICATION OF PRISMATIC DISLOCATION DEFECTS BY ELECTRON MICROSCOPY

Permalink
https://escholarship.org/uc/item/8ht2q2j5

Authors
Thomas, G.
Bell, W.L.

Publication Date
1965-08-01

University of California

Ernest O. Lawrence Radiation Laboratory

IDENTIFICATION OF PRISMATIC DISLOCATION DEFECTS BY ELECTRON MICROSCOPY

Berkeley, California

DISCLAIMER

UNIVERSITY OF CALIFORNIA

Lawrence Radiation Laboratory
Berkeley, California

AEC Contract No. W-7405-eng-48

IDENTIFICATION OF PRISMATIC DISLOCATION DEFECTS
BY ELECTRON MICROSCOPY

G. Thomas and W. L. Bell

August, 1965

IDENTIFICATION OF PRISMATIC DISLOCATION DEFECTS

BY ELECTRON MICROSCOPY[*]

G. Thomas and W. L. Bell

Department of Mineral Technology, College of Engineering,
University of California, Berkeley

ABSTRACT

Two techniques viz., diffraction and strain contrast for identifying large and small prismatic dislocation defects by transmission electron microscopy are described. Large defects can be analyzed by inspection. If the defect is a pure edge loop, the dislocation will have uniform contrast and, if faulted, characteristic fringe contrast will be observed. If loops are not pure edge, a double-arc dislocation image occurs containing a line of weak contrast that is always normal to the (projected) Burgers vector. Examples for FCC, and BCC crystals are given. If the defect is large enough, the plane containing the dislocation loop can be identified. A new method involving simple tilting experiments away from the $s = 0$ condition in dark field is described which enables the sense of the defect to be determined (i.e., vacancy or interstitial).

For defects too small to be adequately resolved by diffraction contrast, dark field strain contrast imaging must be used. It is shown how various kinds of possible defects can be distinguished, and the conditions required to produce and identify strain contrast images are described.

A. INTRODUCTION

Prismatic dislocation defects are defects which lie on the prismatic surface containing the dislocation line and its Burgers vector. They are formed as a result of interactions between point defects and/or dislocations. The most common kinds are dislocation loops formed from clustered point defects (e.g., by quenching, irradiation or plastic deformation) prismatically punched loops from inclusions, and loop and dipole debris left behind moving dislocations (e.g., by tensile, fatigue or creep deformation). A non-planar dislocation defect is the tetrahedron observed in FCC metals of low stacking fault energy. No other kinds of dislocation defects have been observed as yet. This paper will be concerned with the identification, by electron microscopy and diffraction, of such prismatic defects. Experiments are described which allow different types of defects to be distinguished, and it is hoped that the paper will be useful to those who are investigating the structures of quenched, irradiated or deformed metals. The paper is not intended as a review of all the observations that have been made of prismatic defects, but typical references are given where appropriate.

The problem of image detection and analysis by electron microscopy involves two similar contrast mechanism, viz., diffraction contrast and strain contrast, both of which have been theoretically treated in terms of the dynamical theory of electron diffraction for two beam orientations.[1-3] The former mechanism applies to large, resolvable defects and is the normal way by which defects are observed. Diffraction contrast arises due to the fact that the atomic displacements around a defect modifies the parameter s (the deviation from the ideal Bragg condition in reciprocal space) and

introduces a phase change in both transmitted and diffracted waves. The position of a dislocation image depends on the sign of the product $(\bar{g}.\bar{b})s$ where $\bar{g}$ is the reciprocal lattice vector of the operating reflection and $\vec{b}$ the Burgers vector of the defect. When $(\bar{g}.\bar{b})$ is zero, defects are invisible or show weak contrast.[1,2] Once $\bar{g}$ is uniquely determined, and since the sign of s is known from the diffraction pattern, the relative position of the image can be used to find the sense of $\vec{b}$ and hence determine whether defects are vacancy or interstitial in character (for review of diffraction contrast see ref. 4). This method has been widely used for studying prismatic loops and involves controlled tilting experiments using a goniometer stage.[5] A simpler method for the analysis of large defects will be described here.

Although diffraction contrast is suitable for analysing large defects, it is not useful for studying small defects. For dislocation loops smaller than about 200Å, the images of their sides are not resolvable (the dislocation image width is ~ 100Å). Also, the strain field of the loop is markedly affected due to interactions of the various segments of dislocation line surrounding the loop. Similar effects occur with small three-dimensional defects. In these cases strain contrast imaging must be used and has been successful in identifying perfect and imperfect loops in quenched and irradiated copper.[6,7]

Strain contrast images are obtained from defects when the crystal is oriented close to the ideal Bragg condition ($s \approx 0$). The images appear as black-white regions divided by a line of no contrast.[3] Under suitable diffracting conditions, the sense of the displacement is found by inspection, e.g., for vacancy defects the bright side of the image is in the same

direction as that of $\vec{g}$ (dark field image, positive print). The parameter $\bar{g}.\bar{b}$ is still important in modifying s, although s itself does not usually play a major role in the contrast mechanism. Again if $\bar{g}.\bar{b}$ is zero, weak or no contrast will be observed. Very small localized strain fields can be detected by strain contrast but which may not give rise to any significant diffraction contrast. It is emphasized that while bright field imaging at the s > 0 condition for maximum contrast is adequate for the analysis of large defects, dark field imaging at s ≈ 0 is more suitable for observing small defects, or defects showing weak diffraction contrast. For maximum resolution and contrast, dark field images must be obtained by gun tilting as described elsewhere.[6] It must be remembered that after gun tilting the orientation of the specimen is unchanged but the direction of $\vec{g}$ is reversed compared to bright field.

There is much confusion in the literature concerning the so-called small "black spot" defects (bright field images) because it is impossible by inspection to decide whether these are three-dimensional defects, loops, or end-on dislocations. However, in the dark field image near s = 0, it is easy to distinguish between these possibilities by noting the type of black-white contrast and the relation between the line of no contrast and that of the direction of $\bar{g}$. Care must also be exercised when investigating these small defects, as they can be produced as a result of ion damage inside the microscope.[9,10]

For analysis of defects by contrast work, two beam orientations must be obtained, and this is facilitated by using a goniometer tilting stage. Also, the correct orientation between image and diffraction pattern(180° plus the magnetic rotation) must be allowed for before attempting analysis.

(For review see ref. 4). These conditions have all been met in the examples used in this paper.

This paper will be in two parts. The first part is concerned with the identification of resolvable defects by diffraction contrast and is based on recent investigations of loops in quenched FCC metals.[8] A model is described which enables most defects to be identified by inspection, and in FCC crystals there is no need for $\bar{g}.\bar{b} = 0$ contrast experiments. The second part describes the use of dark field strain contrast imaging for identifying small defects.

B. DIFFRACTION CONTRAST FOR LARGE DEFECTS

1. Prismatic Loops

There are two kinds of prismatic dislocation loops, viz., type 1, a pure edge loop with Burgers vector normal to the loop and type 2, a mixed loop with Burgers vector inclined to the plane of the loop. Well known examples of these in quenched FCC metals are: Type 1(a) the Frank or imperfect loop enclosing a stacking fault with $\vec{b} = a/3 <111>$ and type 1(b), the diamond shaped (rhombus) loop with $\bar{b} = a/2 <110>$ which is nearly perfect edge since the habit plane is near {110}. Climb sources also belong to the latter category, with the loop planes variable but usually {001} or {011} with $a/2 <110>$ Burgers vectors. Type 2 loops are perfect loops on {111} with $\bar{b} = a/2 <110>$ (see refs. 11-13 for reviews). Examples of these various defects are shown in Figs. 1-4,7,10. It will be noticed that the type 2 loops are characterized by double-arc images whose lines of no (or weak) contrast are always along $<110>$ directions in FCC and BCC crystals (e.g.,Fig. 12). This line is referred to as LC in this paper. Type 1 loop is immediately recognized from the image. Type 1(a) is a

loop enclosing a stacking fault for which the characteristic extinction fringes are observed if the loop is larger than the extinction distance for the operating reflection[1] (Fig. 1a). Type 1(b) does not contain a stacking fault but, because it is pure edge, the dislocation forming the loop is always in good contrast at all positions. Such loops are different from type 2 loops which exhibit double arcs and so can also be identified by inspection (Figs. 1a,b).

In some cases, e.g., gold, tetrahedral defects are observed (Fig. 1d) which have characteristic projected tetrahedral shapes and associated fringe patterns.[9,14-18] These defects can be distinguished from triangular Frank loops in that the latter have $\vec{b} = a/3$ <111> while the tetrahedron is bounded by $a/6$ <110> edge partials, and so suitable $\bar{g}.\bar{b} = 0$ contrast experiments can be performed for identification[9] as illustrated in Fig. 1(e). Also the choice of suitable orientation facilitates observation, e.g., in [001], tetrahedra project as squares (Fig. 1(d)) while Frank loops project as triangles or hexagons (Fig. 1(a)).

The FCC rhombus loops (Fig. 1(a)) form by climb, glide and/or rotation (for review see ref. 19). Whilst they would be expected to rotate from (111) to (110) to become pure edge, previous observations show that {110} <110> loops are not very common, confirming the theoretical predictions of Bullough and Foreman.[20] In Fig. 1(a) the orientation is determined by Kikuchi analysis[21,22] to be [013] and the rhombus loops lie on several planes. Those marked R to the left of A lie close to (10$\bar{1}$) and are nearly pure edge and so have uniform contrast. Loop A, however, has not yet rotated into the pure edge orientation as shown by its line of no contrast. From the geometry of the loop it lies very near (3$\bar{1}$3), with sides along [$\bar{1}$32] and [$\bar{2}$$\bar{3}$1]. There are also weak residual contrast ($\bar{g}.\bar{b} = 0$) images

from both diamond loops on (0$\bar{1}$1) and perfect loops on ($\bar{1}\bar{1}$1) with $\bar{b} = \frac{a}{2}$ [011].

Examples of (nearly) edge prismatic loops are also expected in BCC and HCP

metals, but, compared to FCC metals, relatively few observations have been

made in these systems.

Type 2 loops are commonly observed in quenched, irradiated, and de-

formed FCC, BCC, and HCP crystals (e.g., refs. 1,5, 11-13, 23-27) as well

as in deformed and annealed MgO.[28] A model has been devised to explain

the origin of double-arc contrast from perfect loops in FCC crystals and

which has been verified experimentally.[8] We shall review the model again

and show its applicability to other crystal systems.

2. Double Arc Perfect Loops in FCC Crystals

Figure 5(a)(b) shows the view normal to the plane containing a Frank

loop (a) and the perfect loop (b) in FCC crystals. The dislocations bound-

ing the loops will tend to lie along the three <110> directions shown; the

perfect loop has $\bar{b}$ = a/2 [110], hence the segments along [1$\bar{1}$0] are pure

edge segments while the segments along [10$\bar{1}$] and [01$\bar{1}$] are mixed disloca-

tions. It can be seen from Fig. 5(c) that the extra half planes of the

perfect loop lie above the loop along one edge and below it at the opposite

edge. The mixed segments can thus be regarded as resolved edge dislocation

dipoles whose separation is a minimum at the two corners formed by the

junction of the [10$\bar{1}$] and [01$\bar{1}$] segments. At these corners the contrast

will be expected to be a minimum because the strain fields cancel to some

degree. The contrast then improves with distance from the corners and

becomes a maximum along the two pure edge segments parallel to [1$\bar{1}$0]. Thus,

the double-arc loop in FCC metals is characterized by a line of no contrast

(LC) along that [1$\bar{1}$0] direction which is normal to the Burgers vector.

This line is normal to the [11$\bar{2}$] direction (referred to as the D axis).

In a micrograph the projected <110> directions (which form a tetrahedron) can be obtained from a suitably oriented stereogram corresponding to the foil orientation. The latter should be obtained as accurately as possible, preferably from Kikuchi diffraction analysis.[21,22] The lines of no contrast are identified by comparison to the projection (see Fig. 2(b)) and since each <110> direction is normal to only one other <110> direction, the Burgers vector is obtained by inspection.[8] The loop plane is one of the two {111} containing the [110] line of no contrast, hence the number of possibilities is reduced from four to two. Further inspection of the [112] projections usually enables the loop plane to be identified uniquely, since only one [112] is normal to the [1$\bar{1}$0] line of no contrast. Any discrepancy from this indicates that the loop plane is no longer one of the {111}.

Figure 6(a) shows a summary of the possibilities for perfect double-arc loops in FCC for the four lowest index orientations. Comparison of actual images to such diagrams is usually sufficient for unique identification.

Perfect loops in HCP crystals are also expected to show double-arc contrast. We have observed such loops in deformed magnesium, but a comlete analysis of all the possible cases has not yet been carried out.[+] Faulted loops on (0001) with Burgers vector [0001] will appear exactly like Frank loops in FCC (Fig. 1(a)) and show uniform dislocation contrast around

---

[+] Rau (private communication) has observed prismatic loops on prism faces in irradiated BeO. Such loops have LC parallel to the $\bar{c}$ axis with $\bar{a}$ Burger's vectors as predicted by the double-arc model.

the loop and fault fringes within the loop if it is larger than the extinction distance for the operating reflection.

3. Double Arc Non-Edge Prismatic Loops in BCC Crystals

The normal Burgers vector in BCC systems is a/2 <111> and since dislocations will always tend to lie along the close packed directions, the perfect loop is expected to lie on {110} (as these contain the two shortest equilength <111>) with the major axis along [110] and the minor axis along that [001] which is normal to the major axis. The Burgers vectors are one of the two <111> possibilities each at 55° to the loop plane. The {112} planes are unlikely habit planes because only one <111> direction is contained by this plane and no <001> direction which is the next shortest vector to <111> in BCC systems. However, the (001) <111> is also a possible prismatic system. Loops on this system are expected to be square, with sides along the two <001> directions. In deformed metals, however, the loops or dipoles can have any shape depending on their mechanism of formation. Unlike the {111} <011> loops in FCC, neither {110} <111> nor {100} <111> contain a pure edge segment. Nevertheless, similar arguments apply in that the extra half planes corresponding to the edge dislocation components lie above and below the loops about one of the <110> axes of the loop, and, hence, dipole relaxation will occur at one of the sets of opposite corners. Thus, as in FCC systems, the lines of no contrast are also along <110> and, in fact, are the <110> normals to the projected a/2 <111> Burgers vector, both for {011} and {001} loops. Hence, the <110> projected tetrahedron serves for both FCC and BCC systems. In the BCC systems the loop plane can be uniquely identified but for {110} loops, each loop has two possible Burgers vectors

and for {001} loops there are four possible Burgers vectors all of which are symmetrical about the loop plane.

Eyre and Bullough[29] have also considered the types of prismatic loops that are possible in irradiated BCC metals and predict {110} loops with $\vec{b} = a/2 \langle 111 \rangle$ or a $\langle 001 \rangle$. The a$\langle 001 \rangle$ loops have been observed in quenched molybdenum[30] and irradiated iron,[27] and several workers have identified loops with $\vec{b} = a/2 \langle 111 \rangle$.[25-27] Eyre and Bullough, on the basis of elastic energy considerations, concluded that both the a/2 $\langle 111 \rangle$ and a $\langle 001 \rangle$ loops are initially rectilinear and lie on {110} but should grow into circular loops and rotate into the pure edge orientation, just as perfect loops do in FCC metals (Fig. 1(a)). However, the $\langle 001 \rangle$ BCC loops usually retain square shapes probably because of the reduction in core energy when the loop sides lie along the $\langle 100 \rangle$ directions in the $\langle 001 \rangle$ plane.[29] Such changes can be detected in the microscope, since the {001} $\langle 111 \rangle$, {011} $\langle 111 \rangle$, or {011} $\langle 001 \rangle$ (non-edge type) loops should show lines of no contrast and these lines should disappear if the loops rotate into the edge orientation (as for rhombus loops in FCC, Fig. 1(a)).

Figures 8(a),(b) show the double-arc contrast expected from perfect loops in BCC metals. The basic geometrical features for FCC and BCC loops are summarized in Table 1.

4. <u>Determination of the Sense of the Loop (Vacancy or Interstitial)</u>

The method involves the relation of the image to the parameters g and s. Various techniques have been described for determining the sense of the loop (vacancy or interstitial), none of which are particularly convenient as they either involve difficult large angle tilting experiments,[5,28] or removing the foil for x-ray identification,[31] since it is necessary to obtain the unique direction of $\bar{g}$. In an arbitrary spot diffraction pattern,

unless a Kikuchi pattern is also present, the choice of plus or minus g

vectors is arbitrary. We have found a simple way of determining the unique

orientation for the general situation (i.e., when Kikuchi analysis is not

possible), which involves determining the top or bottom surface of the

foil.[8,32] The rules that govern the intensities at the top or bottom are

the following: in dark field the contrast of a slip trace, dislocation

line, stacking fault or any defect either extending through the foil, or

lying close to either surface, is strongest at the top of the foil for

s negative and at the bottom for s positive under conditions where absorp-

tion contributes to the image (i.e., in thick regions). This is illustrated

for stacking faults in Fig. 9 and Frank loops in Fig. 10. This rule can be

used to determine approximately the depth in the foil at which defects are

located (see also Fig. 16). Thus, after a foil is examined it is necessary

only to find an inclined extended dislocation or cause a slip trace to

occur (e.g., by beam heating) and perform s ≠ 0 experiments in dark field

from which the sense of slope of the loop plane of interest is determined.

If the loop image is taken at s > 0 and the Burgers vector makes an acute

angle with the upward normal to the habit plane, then, if g.b > 0, the image

of a vacancy loop will lie inside, and that of an interstitial loop out-

side, the true projected image of the loop.[1,2,4] The reverse is true for

g.b < 0. An example is shown in Fig. 10 where the loop A lies on ($\bar{1}\bar{1}1$)

sloping downward from bottom right to top left as determined from the dark

field at s ≠ 0 (Fig. 10(a),(c)). Its image is larger in (a) than (c), $\bar{g}$

makes an obtuse angle with $\vec{b} = a/3$ [$\bar{1}\bar{1}1$] and s > 0, hence (g.b) s < 0 so

that loop A must be a vacancy loop, as expected after quenching.

Table 1. Identification of double-arc images from
perfect non-pure edge prismatic loops

Crystal	Loop plane	Number	Burgers vector	Angle between $\vec{b}$ and loop plane	Crystallography of loop[*]	Loop sides
FCC	{111}	(4)	a/2 <110>	54.7°	LC <110> normal to $\vec{b}$	along <110>
					D <112> normal to LC	
	{110}	(6)	a/2 <111>	54.7°	LC <110> normal to $\vec{b}$	along <111>
BCC					D <100> normal to LC	
	{100}	(3)	a/2 <111>	35.3°	LC <110> normal to $\vec{b}$	along <100>
					D <110> normal to LC	

[*] LC refers to direction of line of no contrast and D is the direction of the
opposite diagonal.

5. Experimental Verification of Double-Arc Model

    (a) FCC crystals

        Experimental confirmation of the double-arc model is afforded by the usual tilting experiments to obtain the $\bar{g}\cdot\bar{b} = 0$ condition for invisibility. Figure 7(a),(b) shows an example; in Fig. 7(a) the [020] reflection operates. The same area is shown in Fig. 7(b). Loops A, which are visible in (a), have their LC along [110], predicting that the Burgers vector should be $a/2$ [$\bar{1}$10] and thus should be invisible for $g = [\bar{2}\bar{2}0]$ as is the case in Fig. 7(b). Loops B have lines of no contrast along [$\bar{1}$10] predicting that $\bar{b} = a/2$ [110] so that they should be visible for both the [020] and [$\bar{2}\bar{2}0$] reflections. That this is so can be seen from Fig. 7.

        Many examples of double-arc loops have already been discussed in detail elsewhere,[8] so only a few illustrations will be used again here.

        Figure 2(a) shows double-arc loops in quenched aluminum. The foil orientation is [013] and the corresponding <110> projections are shown in the stereogram of Fig. 2(b). Loop A has its LC projected along [110], hence its Burgers vector = $a/2$ [$\bar{1}$10]. The projection of the D axis lies along [$\bar{1}$21] or [1$\bar{1}$2]. However, only [1$\bar{1}$2] is normal to [110] (Table 1), hence the loop plane is ($\bar{1}$11).

        Figure 3 illustrates the use of Fig. 6 for identifying the loops. In (a) the loop must be loop A on (111) with $\vec{b} = a/2$ [110] and the inclined loop in (b) must be loop B with $\bar{b} = a/2$ [$\bar{1}$01] on (1$\bar{1}\bar{1}$). In Fig. 1(a) faint double-arc loops are observed, so the Burgers vector must lie at a small angle to the incident beam, whence $\bar{g}\cdot\bar{b} = 0$ for diffraction contrast. However, the displacements normal to the Burgers vector (along [001]) can be utilized to form a strain contrast image. This is shown in Fig. 4 for

dark field under diffraction contrast (a) and strain contrast (b). In

Fig. 4(b) the sharp lines of no contrast for the two loops are normal to

[001] as expected.[8] It should be noted that pure edge loops where $\bar{g} \cdot \bar{b} = 0$

may also give rise to apparent lines of no contrast. However, these lines

will always be normal to $\bar{g}$ and are easily distinguished from non-edge loops.

During observations of climb, the unfaulting of Frank loops can

immediately be detected by the change in contrast to double arcs. Other

examples of double-arc loops have been observed in deformed metals and many

examples exist in the literature (e.g., ref. 23). Figure 11 shows examples

of dipoles and double-arc loops formed in ultrasonically irradiated aluminum.[33]

The lines of no contrast all lie parallel to <110> projections. For example,

loop A has LC along [110], D along [1$\bar{1}$2], hence the loop plane is ($\bar{1}$11) with

Burgers vector a/2 [1$\bar{1}$0].

(b) BCC metals

The excellent agreement between the double-arc model and observations in

FCC metals was also found for BCC metals. Both {011} <111> and {001} <111>

type loops have been identified. Figure 12(a), (b) shows examples of the

latter case observed in Nb tensile defromed 5% (compare to Fig. 8). The

small loop in (a) fits very well for a (100) loop with Burgers vector

$\frac{a}{2}$ [1$\bar{1}$1] or $\frac{a}{2}$ [$\bar{1}$11]. Similar examples are shown in (b) where the loops are

elongated into dipoles. Figure 12(c) shows numerous double-arc dipoles,

also in Nb, after 10% tensile deformation. The loop systems, A, C, D can

be identified with the <110> lines of no contrast shown in the inset. Those

marked A correspond to (011) loops with $\vec{b} = \frac{a}{2}$ [111] or $\frac{a}{2}$ [$\bar{1}$11]. Similar

results apply to the loops shown in Fig. 13 obtained from deformed tantalum.

The circled double-arc loop has LC along [$\bar{1}$01] and D along [010] so the loop

plane is probably (101), with Burgers vector a/2 [$\bar{1}$11] or a/2 [1$\bar{1}$1].
Since $\bar{g}$ = [$\bar{1}$10] any loops with $\bar{b}$ = a/2 [111] or a/2 [11$\bar{1}$] are invisible.

In the BCC case, each double-arc loop can either have two possible
a/2 <111> Burgers vectors both of which are normal to the <$\bar{1}$10> lines of
no contrast. Which of the two actually exist can be decided in the usual
way from tilting experiments to find the $\bar{g}$.$\bar{b}$ = 0 situation. Thus, whilst
the loop plane can be identified, the unique Bergers vector cannot usually
be obtained by inspection of the image as it can for FCC crystals.

Pure edge loops are also possible in BCC metals. These would be of
the type {001} <001> or {110} <001>, i.e., loops whose Burgers vectors are
normal to the loop plane. Evidence for the former has been found[30] and will
be discussed in the second part of this paper.

There has been only one report of observations of defects in quenched
BCC metals (Meakin et al.[30]). Figure 14(a) is an example. The foil is
near [012] and the inset shows the <110> projections. The strong double-
arc loops have their LC along [10$\bar{1}$] and D along [010], these being the only
directions possible for loop diagonals, so the loop plane is ($\bar{1}$01). The
Burgers vector is either a/2 [111] or a/2 [$\bar{1}$$\bar{1}$1] but since $\bar{g}$.$\bar{b}$ = 0 for [111]
the Burgers vector must be a/2 [$\bar{1}$$\bar{1}$1].

Examples of double-arc loops in Fe^{+} and proton irradiated iron can be
seen in a recent publication by Masters.[27] Masters concluded that the loops
produced by Fe^{+} ions were pure edge type, lying on {100}. A comparison of
his micrographs (e.g., Fig. 3) with Fig. 8(b) of our paper shows that some of
the loops are probably not pure edge but perfect loops of the type {001}
<111>, since the appearance of loops with double-arced images shows that
they cannot be pure edge. The exception arises with apparent double-arc

contrast which occurs from pure edge loops due to residual contrast in orientations where $\bar{g}\cdot\bar{b} = 0$. In this case the LC direction is always normal to $\vec{g}$. Examples can be seen in Fig. 1 of Masters' paper.[27]

C. SMALL DEFECTS AND STRAIN CONTRAST IMAGES

1. General Introduction

Ashby and Brown[3] first demonstrated the usefulness of dark field imaging for the analysis of small precipitates or inclusions. Later Bell et al.[6] and Essmann and Wilkens[7] used the technique to identify small prismatic loops in copper. Tunstall et al.[34] considered the strain contrast images from end-on dislocation images. The results of these investigations and some recent work done in our laboratory provide sets of experimental rules which enables the identification of defects to be carried out unambiguously. These rules are based on dark field images and depend on the shape of the black-white lobed images and the line of no contrast (both of which are characteristic of strain contrast images) with respect to the operating reflection. The rules are summarized in the following:

(1) Plate-like defects give good strain contrast images provided the normal to the plane of the defect lies normal to the incident beam to within about 15°. These images must not be confused with double-arc images or with images from loops whose Burgers vectors are (nearly) parallel to the incident beam[8] (see Fig. 4).

(2) Pure edge prismatic planar defects (i.e., $\bar{b}$ normal to the habit plane) give rise to symmetrical black-white lobed images divided by a line of no contrast normal to the (projected) Burgers vector irrespective of the direction of $\bar{g}$.

(3) Prismatic planar defects whose Burger's vectors are inclined to the habit plane have a streaked black-white image that is not normal to the line of no contrast (except in special orientations[*]). The direction of streaking usually lies parallel to the normal to the habit plane but the line of no contrast always lies normal to the (projected) Burgers vector irrespective of the direction of $\bar{g}$.

(4) End-on dislocation images have black-white contrast lobes which are symmetrical about the line of no contrast. The latter is always <u>parallel</u> to the direction of $\bar{g}$. Plate-like defects would be invisible in this condition because $\bar{g}.\bar{b} = 0$. Unlike small loops, the arrangement of the black-white image depends on the sign of s.

(5) Spherically symmetrical defects have black-white lobed images which are symmetrical about the line of no contrast. The latter is always <u>normal</u> to the direction of $\bar{g}$.

(6) Other three-dimensional defects may appear similarly to those of case 5, but may be recognized by having characteristic shapes depending on the orientation. For example, small tetrahedral defects in [111] foils of FCC crystals exhibit a V-shaped line of no contrast dividing the black-white parts of the image.

---

[*] E.g. in the [001] orientation (cubic) both [111] and [110] lie along the same direction so it is not possible to distinguish between these Burgers vectors. However, if LC lies along [011] parallel to [010], etc., then b must be [011] or [01̄0].

(7) For high order reflections, the relation of the image from
prismatic defects is unique with respect to $\bar{g}$ depending on
the lattice displacements, except when the extinction dis-
tance is an appreciable fraction of the foil thickness (e.g.,
in foils of light elements). Thus, in a positive photo-
graphic print, vacancy type defects have their white images
to the same direction as $\bar{g}$ and vice versa for interstitial
defects. For small prismatic defects this sense of the
image is not affected by the sign of s. This is true whether
or not the images are produced in dark field or bright field,[35]
contrary to the result predicted by the dynamical theory used
by Ashby and Brown.[3]

Figure 15 shows how these main types of defects can be distinguished
by inspection of the images and the direction of $\bar{g}$, and examples are shown
in Figs. 16-21. It may happen that in certain orientations a single photo-
graph may not provide the unique answer. All that is necessary in these
cases is to tilt the foil so as to change to a different operating reflection
and then compare again the two images. Thus, images where LC is neither
normal to, nor parallel to, $\vec{g}$ correspond to planar defects. Hence, in FCC
or BCC crystals any reflection not parallel to a (projected) possible
Burger's vector will uniquely identify the loop.

The use of dark field imaging techniques under two beam orientations
for strain contrast work is particularly important for several reasons.
(1) The position of defects giving rise to strain contrast dark field images
can be approximately located within the foil because of the intensity depen-
dence on depth when s is not zero (as illustrated in Fig. 9).[32] For s

negative, defects near the top are in good contrast, while for s positive, defects near the bottom are in good contrast (Fig. 16). Thus, any depth dependence of the image intensity can be characterized by dark field tilting experiments. (2) The dark field image is symmetrical about s = 0 with maximum diffracted intensity in the center of the contour corresponding to the reflection being imaged. Under this condition all defects can usually be observed (except if $\bar{g}.\bar{b} = 0$). (3) Dark field images obtained by tilting the gun have enhanced resolution over bright field images because of the lower amount of inelastically (background) scattered radiation that is present. The resolution limit for small defects is probably of order 10Å.[3]

Some care must be exercised in interpreting the observed images with those predicted by the dynamical theory as used by Ashby and Brown,[3] as we have found some disagreement between observations and theory. We do not wish to debate these issues now, since here our intention is to provide a set of reliable experimental conditions for identifying defects. Our results[35] which differ from those predicted theoretically are:

(1) Bright and dark field images are identical (i.e., the same black-white sense) from defects lying at all positions with-in the foil except perhaps very near the two surfaces.[*] This result is different from the case of images of dislocation lines near the bottom surface of the crystal where bright field and dark field images are complementary in nature.

(2) Reversals in the sense of the image when the defect is of the same sense (i.e., vacancy or interstitial type) sometimes occur

---

[*] This situation is unlikely to occur because prismatic defects very close to either surface will tend to "anneal" out.

for low order reflections (e.g., [111] in FCC [110] BCC, etc.) but disappears for high order reflections. Thus, to avoid possible confusion in analyzing the type of defect it is recommended that large values of $\bar{g}$ be used.

(3) The visibility (but not the sense) of the strain contrast dark field image depends on the sign of s--those near the top are seen for s < 0 and vice versa for s > 0. At s = 0, defects are visible throughout the foil thickness, so the visibility is not confined to the top or bottom half extinction distances.[32]

Figure 16 shows an example of the effect of s on the visibility of strain contrast images from loops in deformed Ag. The defect M is in good contrast for all three conditions shown, hence it must be located near the center of the foil. Those nearer the top and bottom surfaces are marked T and B, respectively.

(4) Maximum contrast occurs at foil thicknesses of $nt_o/4$ (e.g., see Fig. 18) where n is odd (to = extinction distance for the operating g). This corresponds to a grey background, as one would expect intuitively.

(5) In some cases the sense of the image depends on the product $(\bar{g}\cdot\bar{b})s$, as for diffraction contrast. This effect is associated with larger defects or single dislocation lines which show diffraction contrast.

With the above conditions and rules satisfied experimentally it follows that unique identification of small defects by strain contrast imaging is possible from inspection of one, or at most two, dark field photographs of

the same area. The following describes some applications of these results
to the analysis of prismatic defects in quenched or deformed metals. The
same techniques will apply in the study of substructure in irradiated
materials.

2. Quenched or Irradiated Metals

The degeneration of a supersaturation of point defects can result in
one or more of the following types of lattice defects:

1. Clusters of various shapes, collapsed or "loose"
   (with high local point defect concentration),
   three-dimensional voids.

2. Three-dimensional aggregates, e.g., tetrahedra of
   stacking fault.

3. Planar dislocation defects.

Defects of type 1 can be identified by tilting experiments to change the
direction of $\bar{g}$ (Fig. 15(iv)). So far we have not observed small spherical
clusters of point defects but small tetrahedral shaped defects have been
observed in quenched silver. An example is shown in Fig. 17. It can be
seen from this photograph that in addition to the small tetrahedral defects
marked T (compare to Fig. 15(v)), planar defects characterized by images
shown in Fig. 15(i) and (ii) also exist. These are perfect {111} <011>
loops marked P and Frank loops marked F (compare to Fig. 18). In bright
field such small defects appear as black dots when viewed away from the
ideal Bragg orientation and cannot be identified (see, e.g., ref. 13).
This emphasizes the necessity of using dark field techniques for analysis.

Table 2 summarizes the case of prismatic loops in FCC and BCC
crystals. Figure 18 illustrates how the dark field image distinguishes
between Frank loops A, C and perfect loops B, D in quenched copper (FCC).

Table 2. Strain contrast images from prismatic loops in
FCC and BCC metals[1]

System	Loop plane	Burger's vector	Image characteristics[2]
FCC[3]		<111>	LC normal to <111> proj.; image symmetrical about LC, i.e., streaked in <111>
	{111}	<110>	LC normal to <110> proj.; image skewed about LC in <111> proj. direction[4]
	~ {110}	<110>	LC normal to <110>; image symmetrical about LC, streaked in <110>[5]
BCC	{001}	<001>	LC normal to <001>; symmetrical image streaked in <001>
		<111>	LC normal to <111> proj.; image skewed about LC in <001>
	{110}	<111>	LC normal to <111>; image skewed about LC in <110>[4]

1. For loops nearly edge-on in the foil.
2. No dependence on direction of $\bar{g}$.
3. Similar rules apply to HCP crystals.
4. Except in symmetrical cases when [111] [110] coincide; skew direction corresponds to the direction q in Fig. 15. Also, if b is parallel to beam, the direction of LC will be normal to the displacements normal to b.
5. Predicted - no experimental verification available as yet.

More details of these results are published in ref. 6. By comparison, the images of end-on dislocations in aluminum are shown in Fig. 19(a),(b). Here the sense of the image depends on the sign of $(\bar{g}.\bar{b})s$ indicating an appreciable contribution of s, and hence diffraction contrast, to the image. However, the lines of no contrast are parallel to $\bar{g}$, unlike the examples in Figs. 17 and 18. Figure 20 shows examples of strain contrast images from rows of interstitial type planar defects, presumably due to prismatic punching from inclusions, and illustrates the excellent contrast in this case in bright field. That these are planar defects is shown by the fact that $\vec{g}$ makes 45° angles to the LC directions. The orientation here is such that both [111] and [110] are coincident normals to the lines of no contrast. The direction of the black-white contrast shows that the loops must lie on {111} (Table 2) but due to the symmetry it is not possible to uniquely define the Burgers vectors. Thus, in general [001] orientations and similar ones should be avoided if unique identification is needed.

Figure 4(b) illustrates the use of "residual" strain contrast images to resolve defects when $\bar{g}.\bar{b} = 0$. Here the displacements responsible for contrast are normal to $\bar{b}$, i.e., along [001] normal to LC (in FCC metals with $\vec{b} = a/2 \langle 110 \rangle$).

Similar analyses can be applied to defects in BCC metals. Figures 14(b) and 21 show examples of strain contrast images in quenched molybdenum. It can be clearly seen from Fig. 21 that almost all the loops have lines of no contrast normal to projected $\langle 100 \rangle$ with symmetrical images streaked in $\langle 001 \rangle$. These loops are therefore pure edge loops on {001} with $\bar{b} = a$ [001] confirming the results of Meakin et al.[30] However, several loops have their LC normal to projected $\langle 111 \rangle$ (see circled regions of Fig. 21)

and from the direction of the black-white streak they also appear to lie on {001}. Hence, both a <001> and a/2 <111> loops exist after quenching. Similar results are expected to apply to irradiated BCC metals for which, as yet, no strain contrast analyses have been reported.

Figure 14(b) also shows that the majority of the strain contrast images are from loops with $\bar{b} = a$ <100> (e.g., those marked A, while a few have $\bar{b} = a/2$ <111>, e.g., at B.

The analysis of loops in several deformed BCC metals confirm the existence of small prismatic loops with $\bar{b} = a/2$ <111>. Examples can be seen arrowed in Fig. 13. The direction of black-white streaking in these cases suggest both {001} and {110} habit planes.

D. SUMMARY

1. Large Defects

The double-arc model which is proposed to explain the contrast observed from non-pure edge prismatic loops fits observations very well for perfect loops in FCC and BCC metals. Preliminary results indicate that the applicability of our model to HCP systems is also valid. For non-pure edge loops, since the Burgers vectors make acute angles to the dislocation loop, the dipole relaxation that can occur at opposite corners is appreciable, leading to detectable lines of no contrast. These lines of no contrast are always along the long diagonal of the loop (except in {001} <111> BCC loops which are squares, hence each loop can have either of two lines of no contrast (Fig. 8(b)) and this fact can be utilized to study any change in loop plane during climb or glide. An example is the conversion of {111} <011> loops towards {011} <011> rhombus loops in quenched FCC

metals. If the loop goes all the way from {111} to {011}, the major axis
changes from <011> to <100> hence the line of no contrast gradually dis-
appears and a new one appears along the major axis. This new LC gradually
disappears as the pure edge orientation is approached. An example can be
seen at A in Fig. 1(a) where LC lies close to [161] projected. When this
loop was on (1$\bar{1}$1) its line of no contrast would have been along [$\bar{1}$01].
This latter direction is now the short axis of loop A. Loop A must lie
very close to (3$\bar{1}$3). The major axes of loops R to the left of A lie along
[010] projected; these loops do not have lines of no contrast so must be
nearly pure edge and lie on (10$\bar{1}$). We are currently investigating such
loop rotations in more detail.

Determination of the loop plane is possible only when the loop is large
enough so that the directions of the loop sides and axes are resolvable.
For FCC metals, although each possible <110> LC is common to two {111}
planes, the direction of the only possible <112> axis can usually be found
to uniquely identify the loop (as, e.g, in Figs. 2 and 3). The Burgers
vector is immediately found by inspection of the <110> LC directions. In
BCC metals the loop plane can be identified but each plane has two possible
$\frac{a}{2}$ <111> Burgers vectors and further tilting experiments to find $\bar{g} \cdot \bar{b} = 0$
are required.

Both the habit plane and its sense of slope must be known before it
can be decided whether the loops are vacancy or interstitial in character.
We have shown how simple tilting experiments in dark field about the s = 0
position can be used for such determinations. The solution of Kikuchi
electron diffraction patterns also enables the orientation to be obtained
uniquely. Both vacancy and interstitial perfect loops are expected to

to show lines of no contrast and so exhibit a double-arced appearance. Although we have not yet specifically investigated interstitial loops, double-arced loops can be seen in other published micrographs (e.g., in refs. 5, 31).

A pure edge loop parallel to the plane of the foil, observed by residual contrast (i.e., diffraction contrast from $\vec{g} \cdot \vec{b}_p$, where $\vec{b}_p$ are resolved displacements normal to $\vec{b}$) may also exhibit double-arc contrast if the residual strain on parts of the loop is normal to $\bar{g}$ (see e.g., refs. 23, 36). This is a trivial case, however, and is recognizable by the fact that LC is always normal to $\bar{g}$. When large perfect loops are viewed edge-on with $\bar{b}$ in the plane of the foil, the line of no contrast is parallel to the viewing direction and the image appears as two dots separated by a line of weak or no contrast.[8]

In FCC metals, Frank loops may also appear to show double-arc contrast.[37] If the loop is small and the diffracting conditions are such that g.b = 0 or ± 1/3, then the loop dislocation image is not visible, but the extinction fringes, if black-white-black, may lead to a double-arc appearance. However, these fringes are always parallel to the foil surfaces and will not satisfy the conditions for true double-arc images (Table 1) except in special cases. If loops do not exhibit double-arc contrast it can be concluded that they are (nearly) pure edge in character.

2. Small Defects and Strain Contrast

When loops, or other prismatic defects, are smaller than about 200Å they appear as black spots in bright field, and away from the ideal diffracting position, and cannot be identified. However, as shown in this paper, the strain contrast image obtained in the two beam dark field condition

near the ideal diffracting position enables the type of defect and its

sense (vacancy or interstitial) to be unambiguously identified by not more

than two photographs using different reflections and noting the sense of

the black-white image, the line of no contrast and the direction of $\bar{g}$.

The dark field image also enables larger defects which are in orientations

giving rise to residual diffraction contrast to be observed more clearly

(e.g., Fig. 4).

In order to avoid possible confusion in interpreting the sense of the

black-white image in terms of vacancy or interstitial defects, the use of

high order reflections are recommended, since it has been found that for

the lowest order reflections, reversals in contrast from the same type of

defect occasionally arise. The reasons for this are discussed elsewhere.[35]

The position in the foil of small defects can be found by tilting experi-

ments about the s = 0 condition in dark field.

ACKNOWLEDGMENTS

REFERENCES

1. P. B. Hirsch, A. Howie and M. J. Whelan, Phil. Trans. Roy. Soc. A252, 499 (1962).

2. A. Howie and M. J. Whelan, Proc. Roy. Soc. A263, 217 (1961); ibid, A267, 206 (1962).

3. M. F. Ashby and L. M. Brown, Phil. Mag. 8, 1063, 1649 (1963).

4. G. Thomas, Thin Films ASM, 227 (1964).

5. D. J. Mazey, R. S. Barnes and A. Howie, Phil. Mag. 7, 1861 (1962).

6. W. Bell, D. M. Maher and G. Thomas, Lattice Defects in Quenched Metals, (Academic Press, Inc., N. Y., 1965), p. 739.

7. U. Essmann and M. Wilkens, Phys. Stat. Sol. 4, K53 (1964).

8. W. L. Bell and G. Thomas, Phil. Mag. (to be published).

9. D. W. Pashley and A. E. B. Presland, Phil. Mag. 6, 1003 (1961).

10. L. M. Howe, R. W. Gilbert and G. R. Piercy, Appl. Phys. (Letters) 3, 125 (1963).

11. M. J. Whelan, Electron Microscopy and Strength of Crystals, (J. Wiley & Sons, N. Y., 1963), p. 3.

12. G. Thomas and J. Washburn, Rev. Mod. Physics 35(4), 992 (1963).

13. Lattice Defects in Quenched Metals, (Academic Press, Inc., N. Y., 1965).

14. J. Silcox and P. B. Hirsch, Phil. Mag. 4, 72 (1959).

15. R. M. J. Cotterill, Phil. Mag. 6, 1351 (1961).

16. T. Mori and M. Meshii, Acta Met. 12, 104 (1964).

17. R. L. Segall and L. M. Clarebrough, Phil. Mag. 9, 865 (1964)

18. D. N. Seidman and R. W. Baluffi, Phil. Mag. 9, 1067 (1964).

19. R. E. Smallman and A. Eikum, see ref. 13, p. 591.

20. R. Bullough and A. J. E. Foreman, Phil. Mag. 9, 315 (1964).

21. M. von Heimendahl, W. Bell and G. Thomas, J. appl. Phys. 35, 3614 (1964).

22. H. M. Otte, J. Dash and H. F. Schaake, Phys. Stat. Sol. 5, 527 (1964).

23. Electron Microscopy and Strength of Crystals, (J. Wiley & Sons, N. Y., 1963).

24. P. R. B. Higgins and A. C. Roberts, J. Less Common Metals 6, 472 (1964).

25. J. D. Meakin, Nature 201, 915 (1964).

26. M. E. Downey and B. L. Eyre, Phil. Mag. 11, 53 (1965).

27. B. C. Masters, Phil. Mag. 11, 881 (1965).

28. G. W. Groves and A. Kelly, J. appl. Phys. 34, 3104 (1963).

29. B. L. Eyre and R. Bullough, Phil. Mag. 12, 31 (1965).

30. J. D. Meakin, A. Lawley and R. C. Koo, see ref. 13, p. 767.

31. J. D. Meakin and I. G. Greenfield, Phil. Mag. 11, 277 (1965).

32. W. L. Bell and G. Thomas, J. appl. Phys. (to be published), UCRL-16264.

33. K. H. Westmacott and B. Langenecker, Phys. Rev. Letters 14, 221 (1965).

34. W. J. Tunstall, P. B. Hirsch and J. Steeds, Phil. Mag. 9, 99 (1964).

35. W. L. Bell and G. Thomas (to be published), UCRL-16271.

36. W. Pfeifer, Phys. Stat. Sol. 3, 145 (1963).

37. J. L. Strudel, F. Vincotte and J. Washburn, Appl. Phys. Letters 3, 148 (1963).

FIGURE CAPTIONS

Figure 1   Examples of prismatic dislocation defects in quenched

FCC metals.

(a)   Aluminum water quenched from 550°C aged 10 min 100°C,

showing three types of defects: Frank loops F, per-

fect loops on {111} P, rhombus loops R. Notice the

lines of no contrast parallel to <110> for all P

loops, and some R loops exhibiting residual contrast.

Orientation near [013] (compare to Fig. 2(b)).

(b)   Rhombus edge dislocation climb sources and double-arc

loops in quenched Al-5% Mg alloy. Orientation [112].

The perfect loops can be identified by comparison

with Fig. 6(b).

(c)   Helical dislocations and perfect loops exhibiting

double-arc contrast along [011] or [0$\bar{1}$1] in quenched

Al-5% Mg alloy. The helices with $\vec{b}$ = a/2 [110] are

invisible.

(d) Large tetrahedra in quenched gold. Overlapping fringe

contrast can be observed at the defects. Orientation

near [001].

(e) Small tetrahedron in quenched Ag showing stair-rod

dislocation contrast. The stair-rod parallel to

$\bar{g}$ =[220]is invisible. Orientation near [111].

Figure 2(a) Double arc contrast from perfect loops in quenched

aluminum. Orientation [013] the inset shows the pro-

jected <110> tetrahedron.

(b) Stereographic projection of [013] corresponding to

(a). Loop A in Fig. 2(a) has LC along [110], hence

$\vec{b}$ = a/2 [$\bar{1}$10]. The D axis lies along [1$\bar{1}$2], so the

loop plane is ($\bar{1}$11).

Figure 3(a,b) Double arc perfect loops in quenched copper, illus-

trating the use of the double-arc model in Fig. 6

to identify defect systems. In (a), the loop A is on

(111) with b = a/2 [110] and (b) loop B is on (1$\bar{1}\bar{1}$)

with $\vec{b}$ = a/2 [$\bar{1}$01].

Figure 4 Dark field images of perfect loops in a [110]

quenched aluminum foil.

(a) s $\neq$ 0 double arc with lines of weak contrast parallel

to [$\bar{1}$10] indicating $\vec{b}$ = a/2 [110], whence $\bar{g}.\bar{b}$ = 0 for

diffraction contrast. The loops are observed by resi-

dual contrast from displacements in [001] normal to $\vec{b}$.

(b) Same loops at s $\simeq$ 0; the strain contrast image shows

sharp lines of no contrast normal to [001].

Figure 5 (a) View normal to the plane of a Frank loop on (111).

Missing B atoms represent the enclosed intrinsic

stacking fault.

(b) Same loop after conversion to a perfect loop with

$\vec{b}$ = a/2 [110]. Extra atoms between A and B positions

are below the loop plane, those between B and C

positions above the loop plane.

(c)   Side view of the loop in (b) showing the extra half

planes above and below the loop about the [1$\bar{1}$0] axis.

Figure 6   Tetrahedra bounded by <110> directions for (a) [001],

(b) [112], (c) [111] and (d) [110] projections and

appearance of {111} <011> perfect loops for each

projected (111) plane. Double lines indicate images

inside and outside the true loop position depending

on ($\bar{g}$.$\bar{b}$)s. Compare to Figs. 1-4.

Figure 7   Verification of double arc model by tilting experiments.

In (a) $\bar{g}$ = [020] and loops A with $\vec{b}$ = a/2 [$\bar{1}$10] are visible.

In (b) $\bar{g}$ =[$\bar{2}\bar{2}$0],so loops A with $\vec{b}$ = a/2 [$\bar{1}$10] are invi-

sible as predicted. Loops B with $\vec{b}$ = a/2 [110] are

visible in (a) and (b). Bright field images of loops in

quenched Al. Orientation near [001].

Figure 8(a)   Scheme showing appearance of double arc loops expected

for {110} <111> prismatic defects in BCC metals. The

lines of no contrast are <110> projections.

(b)   Scheme showing appearance of double arc loops expected

for {100} <111> prismatic defects in BCC metals.   The

lines of no contrast are <110> projections.

Figure 9   Illustrating experiments on stacking faults in silicon

for determining unique foil orientation.

(a)   Bright field s slightly positive.

(b)   Dark field s $\simeq$ 0 comparison to A indicates top of foil

is at T.

(c)   Dark field s > 0, bottom of foil in contrast.

(d)   Dark field s < 0, top of foil in contrast.

Figure 10   Dark field experiments for identifying the sense of

prismatic dislocation loops. a) s > 0, b) s $\approx$ 0,

c) s < 0. Specimen quenched aluminum containing Frank

loops. Loops near the top, middle and bottom are

marked T, M, B. See text for discussion.   Orientation [016].

Figure 11   Double arc loops in aluminum (bright field) after

ultrasonic irradiation; the <110> projections are shown.

Orientation near [123]. Courtesy Phys. Rev. Letters

and Langenecker and Westmacott (ref. 33).

Figure 12(a,b) Double arc loops in niobium (bright field) after 5%

tensile deformation. The loops are of the {001} <111>

type. Orientation near [001]. (compare to Fig. 8b).

(c) Double arc loops in niobium (bright field) after 10%

tensile deformation. Orientation [013]. Loops A, C,

D have LC along <110> indicated by dashed lines in

inset.

Figure 13 Double arc loop (circled) in dark field image of tan-

talum after 10% deformation. The strain contrast images

arrowed show that $\vec{b} = a/2$ <111>.

Figure 14(a,b) Bright field-dark field pair of loops in quenched

molybdenum (courtesy J. D. Meakin). Inset shows pro-

jected directions of <110> and <111>. Double arc loops

are {011} <111>. The strain contrast loops A are {001}

<001>; whilst B have $b = \frac{a}{2} [1\bar{1}1]$.

Figure 15   Sketch illustrating dark field strain contrast images

expected from different defects.

(i)   Symmetrical, pure edge loops; $\vec{b}$ normal to LC

independent of $\vec{g}$ when loop is within 15° of

being edge-on.

(ii)   Loops with $\bar{b}$ not normal to loop; $\bar{b}$ normal to

LC independent of $\bar{g}$, direction of black white

streak $\bar{q}$ is parallel to loop plane normal.

(iii)   End-on dislocations, LC always parallel to $\bar{g}$.

(iv)   Spherically symmetrical defects, LC always

normal to $\bar{g}$.

(v)   [111] view of small tetrahedron; LC has

V-shape.

i-iii, v for vacancy and iv for interstitial defects.

Figure 16   Illustrating the effect of the sign of s in dark field

on the visibility of strain contrast images.   Specimen

Ag 10% cold rolled.   Most defects are vacancy loops.

a) s < 0, b) s = 0, c) s > 0. Defects near the top

marked T, those near the bottom marked B.

Figure 17   Examples of strain contrast images in quenched Ag.

Tetrahedra marked T, perfect loops P and Frank loops F.

Orientation near [111].

Figure 18   Illustrating the use of strain contrast images for dis-

tinguishing between Frank and perfect vacancy loops

in quenched copper. Compare to Fig.15 (i and ii).

Best contrast occurs in grey regions (odd-quarter

extinction distances).

Figure 19   Bright field-dark field pair showing end on dislocations

in aluminum whose LC is parallel to $\vec{g}$. Notice that the

sense of the image is determined by $(\bar{g}\cdot\bar{b})s$.

Figure 20   Bright field images showing strain contrast from

interstitial loops in aluminum formed by a punching

mechanism. Orientation near [001].

Figure 21   Dark field images of vacancy loops in quenched molyb-

denum (courtesy J. D. Meakin). Notice that the majority

of LC lines are normal to $\langle 001 \rangle$ but those circled are

normal to $\langle 111 \rangle$. Some reversals in the sense of the

images occur for the reflection shown.

Fig. 1(a).

ZN-5061

ZN-5213

Fig. 1(b), (c).

0.5 μ
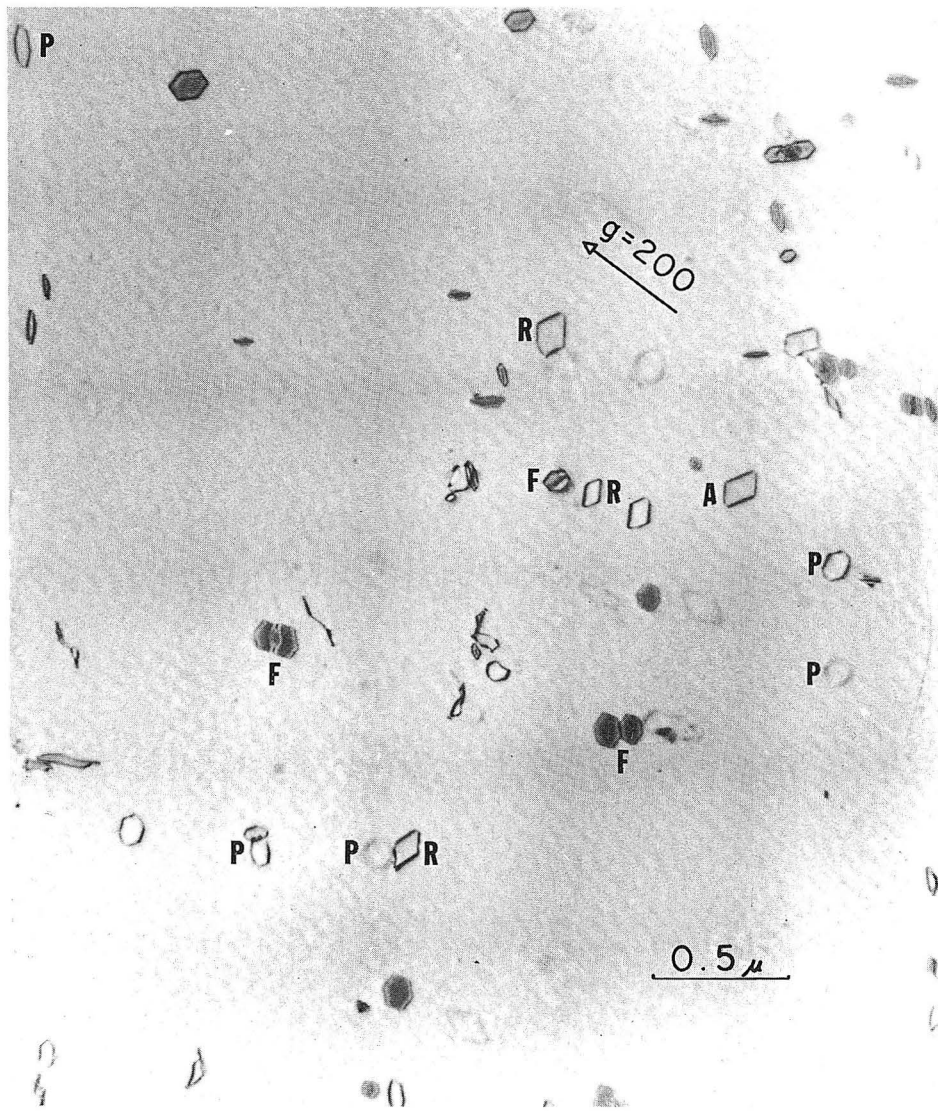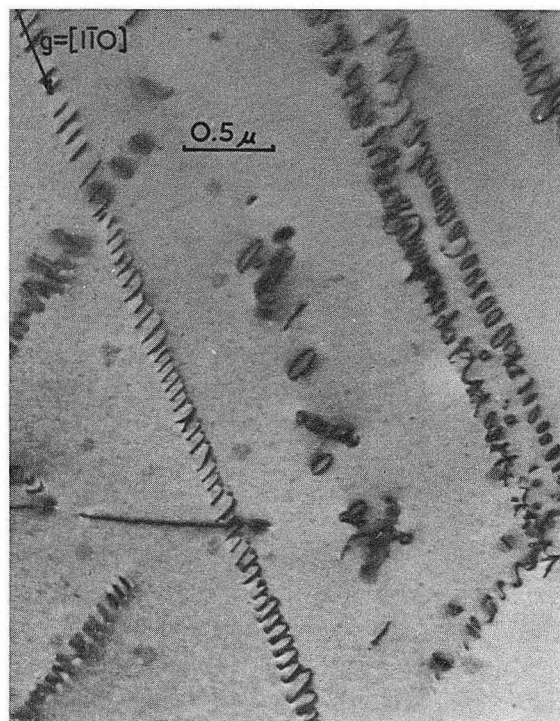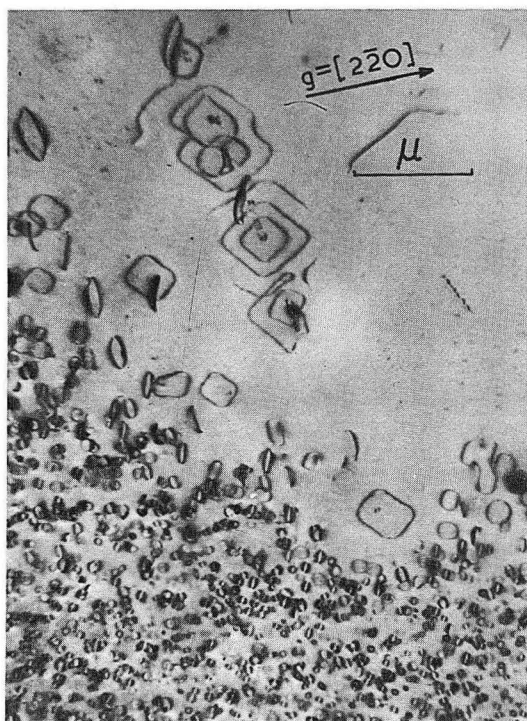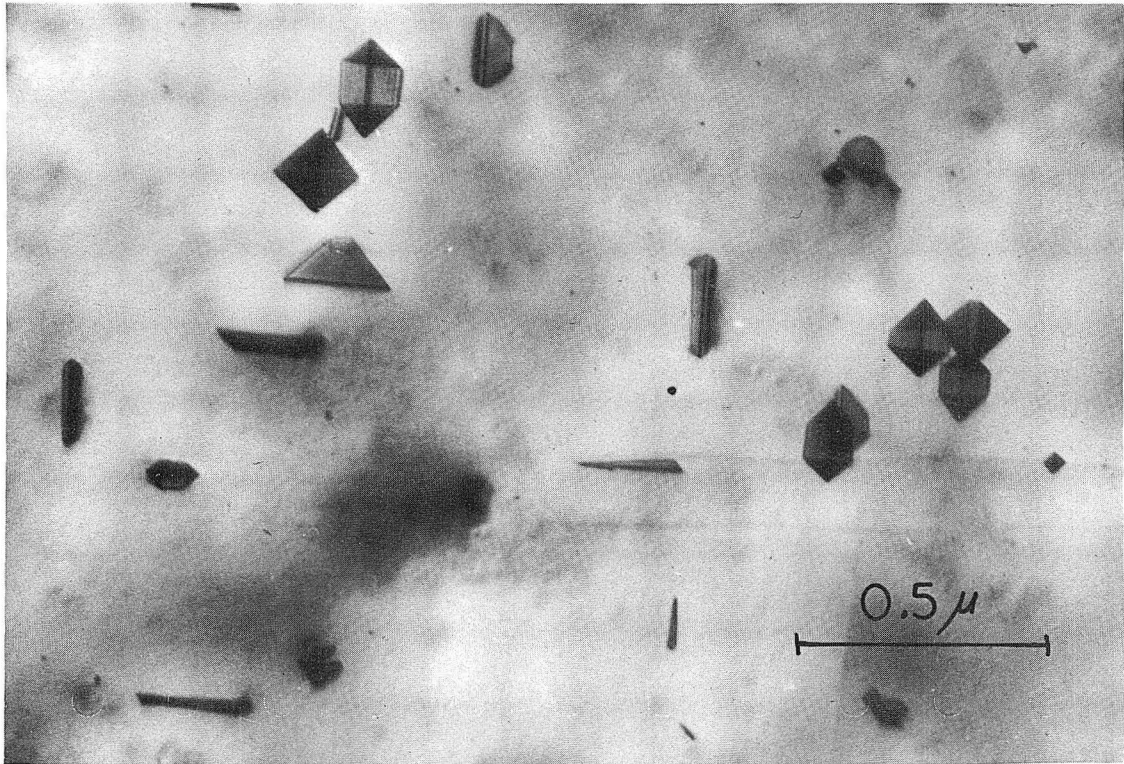
ZN-5218

Fig. 1(d).

ZN-5085

Fig. 1(e).

$\bar{g} \cdot [1\bar{3}1]$

0.25μ

ZN-5224

Fig. 2(a).

(013)

100

[0̄1̄1]

2̄1̄1

110

211

[110]

101

[1̄10]

[101]

1̄1̄1

1̄2̄1

111△

121

112

1̄12

[1̄01]

1̄31

ḡ=[1̄3̄1]

03̄1

010

011

013

100

[011]

0̄1̄1

03̄1

1̄21

.1̄12

.1̄1̄2

△1̄11

1̄2̄1

.1̄01

△1̄1̄1

1̄10

2̄11.

2̄1̄1

1̄00

Fig. 2(b).

(a)

(b)

ZN-4808

Fig. 3.

(a)

(b)

ZN-4799

Fig. 4(a, b).

$[\bar{1}\bar{1}0] \leftarrow$

(a)   (b)

$[10\bar{1}]$ $[11\bar{2}]$ $[01\bar{1}]$

Fig. 5(a, b).

MUB-5618

Fig. 5(c).

(a)   (b)   (c)   (d)

[00I]   [112]   [III]   [IIO]

(III)

($\bar{I}\bar{I}$I)

($\bar{I}$I$\bar{I}$)

(I$\bar{I}\bar{I}$)
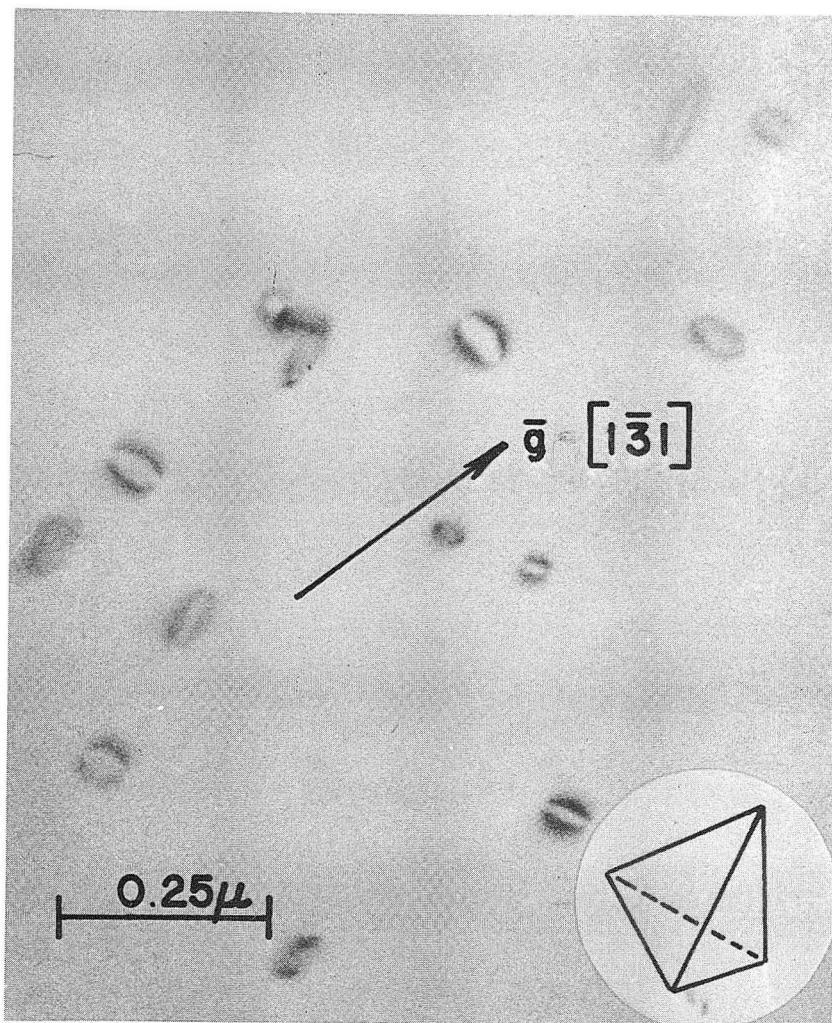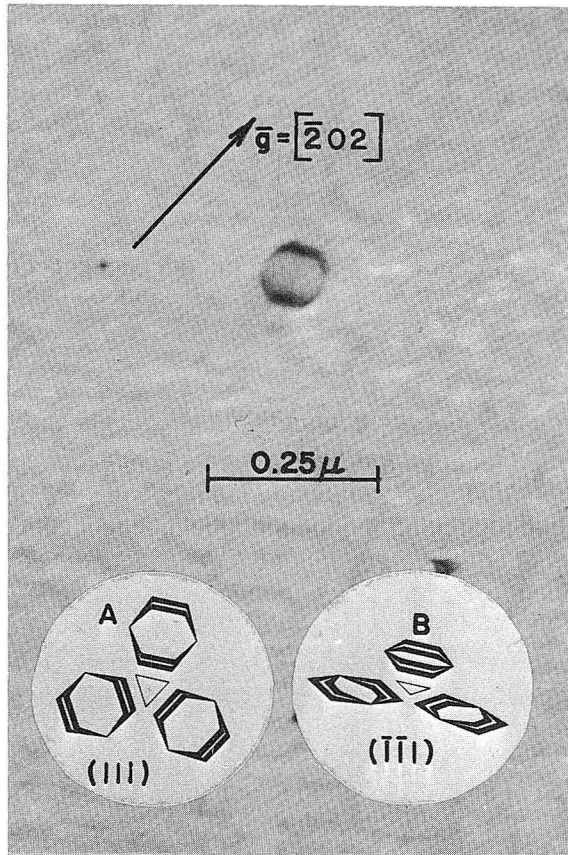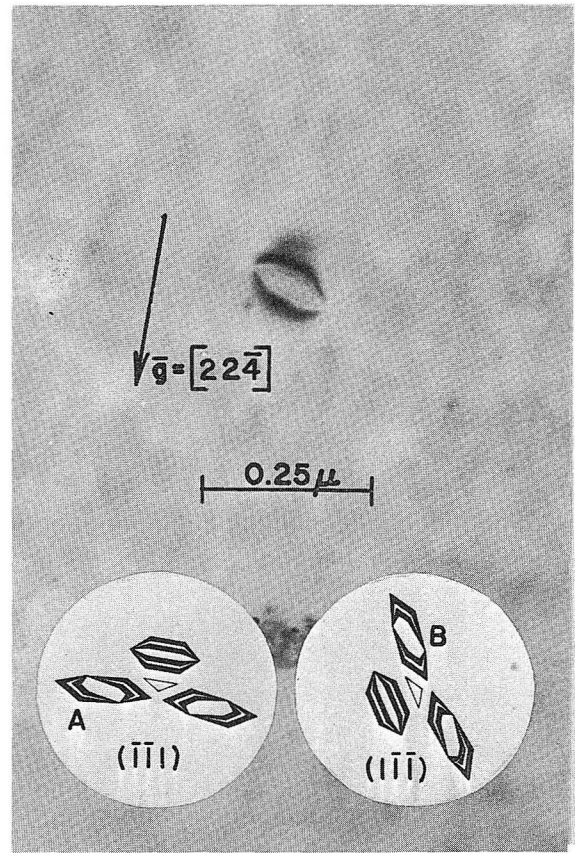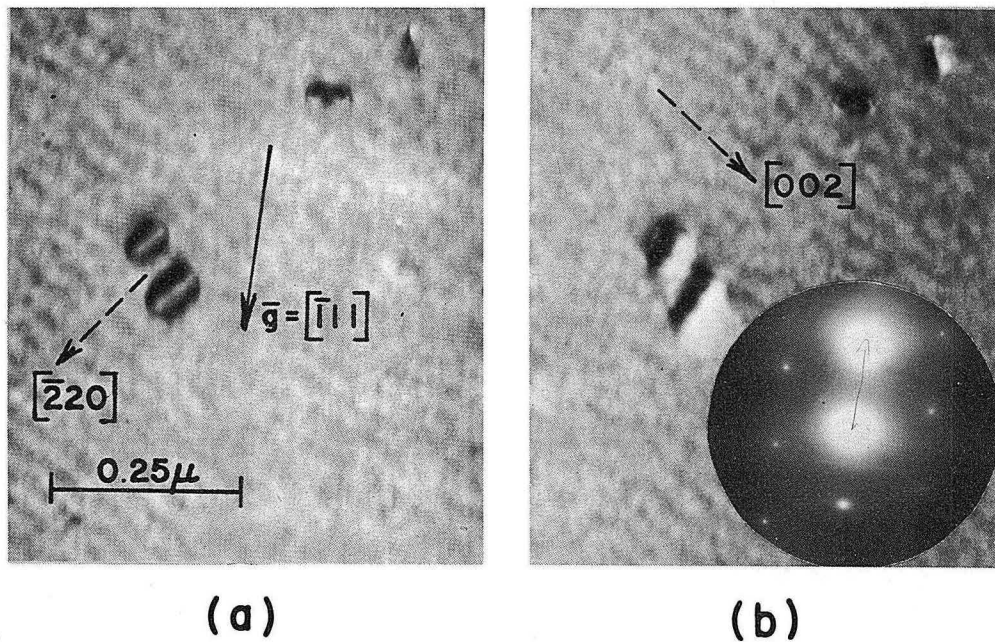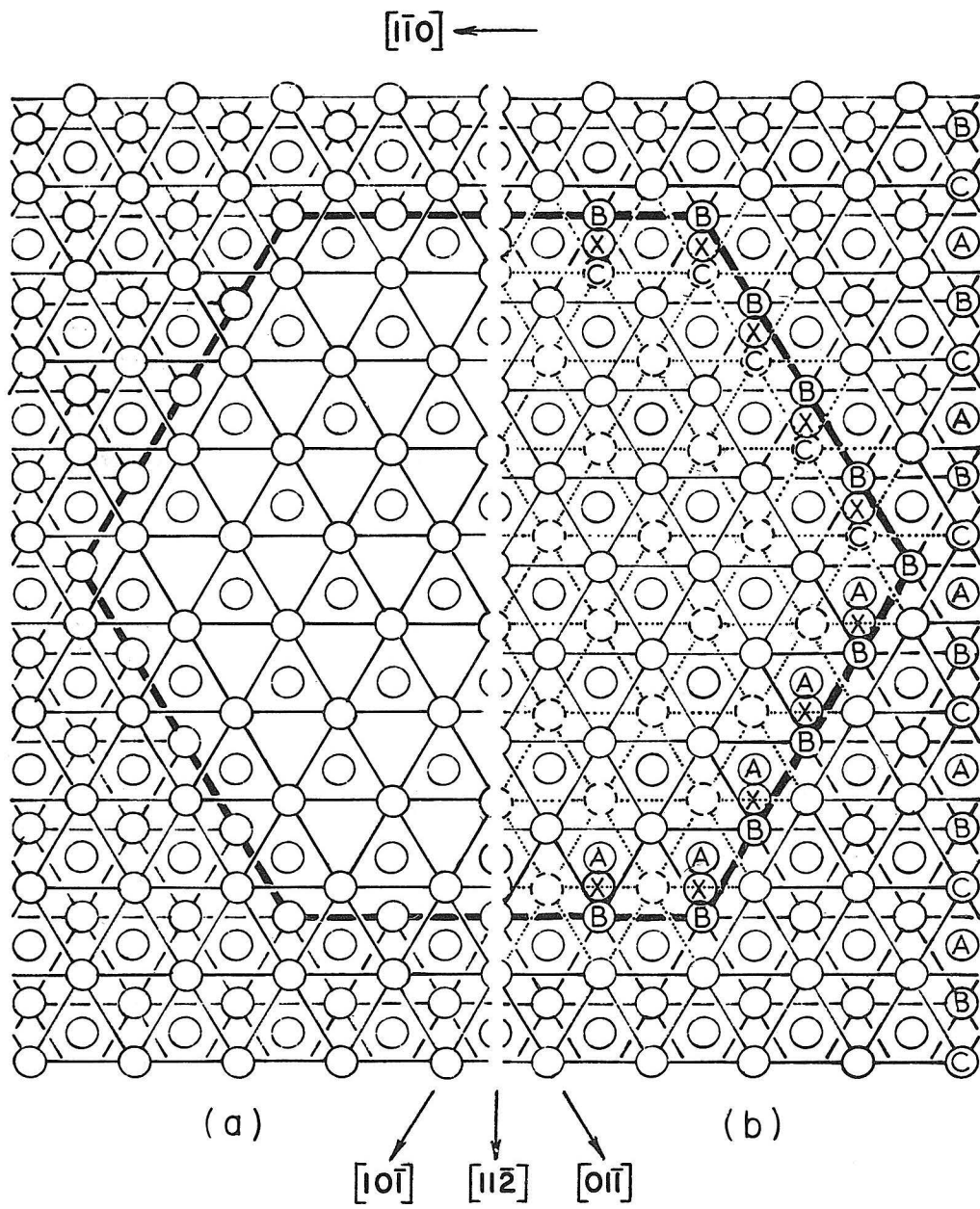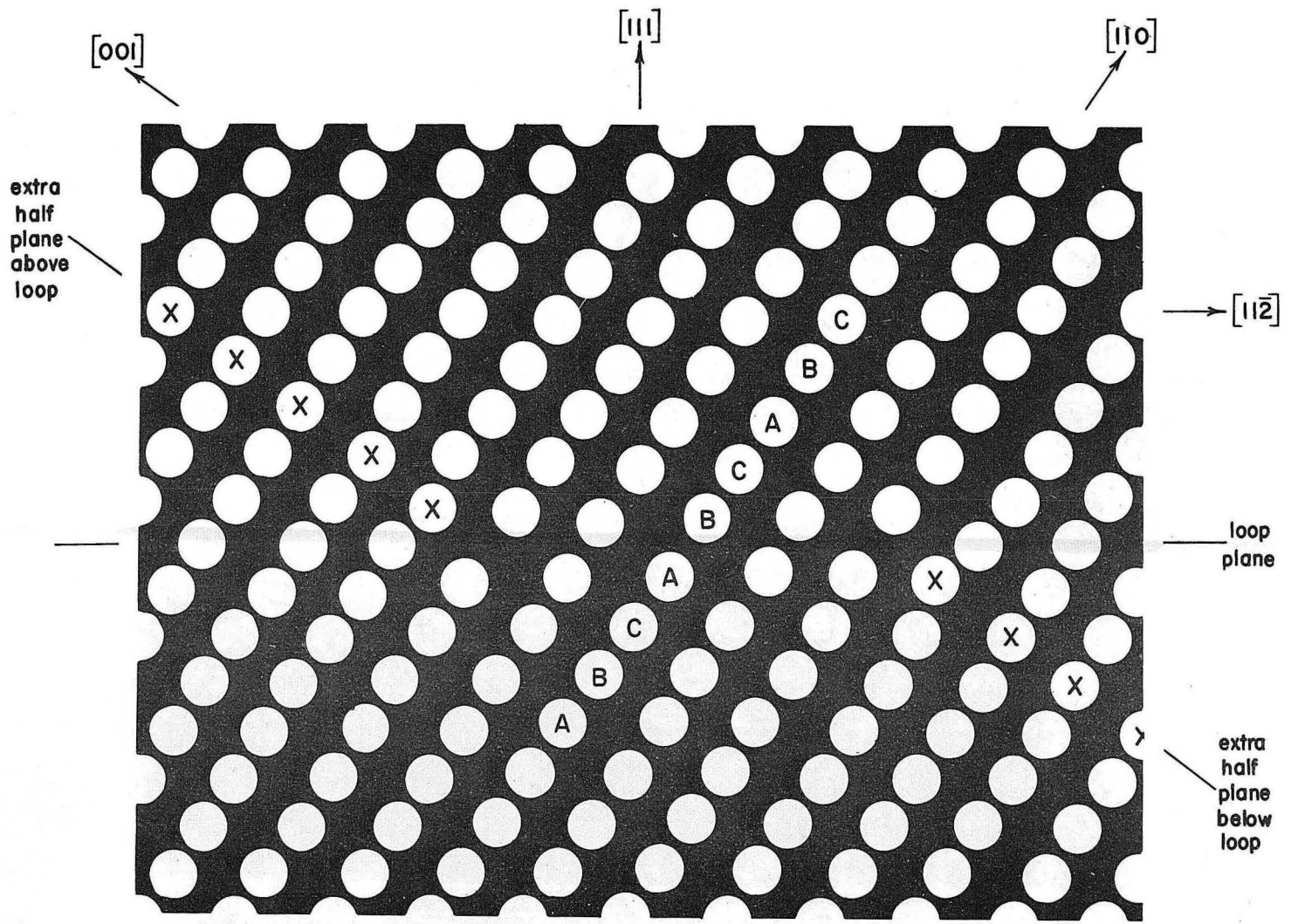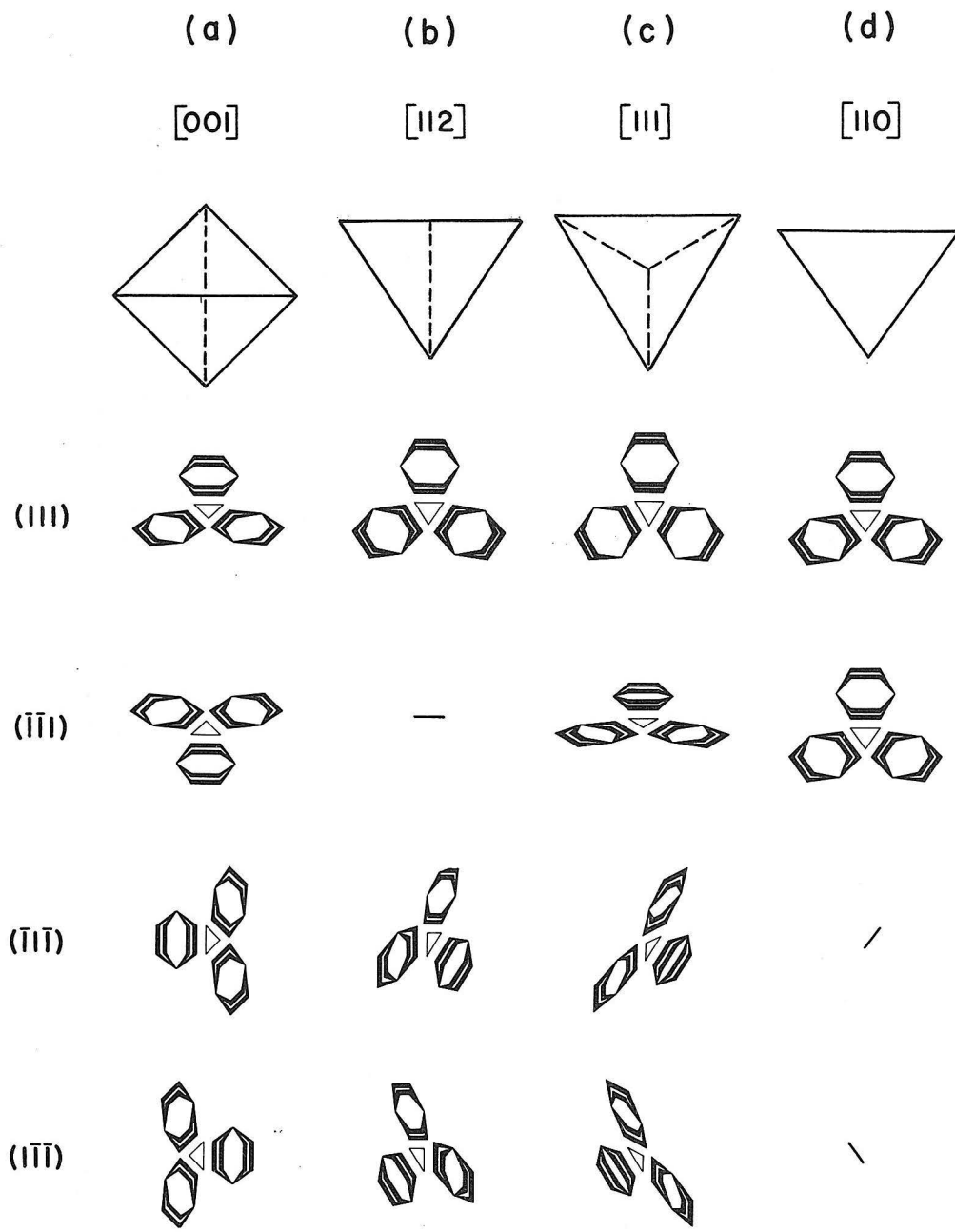
MUB-5621

Fig. 6.
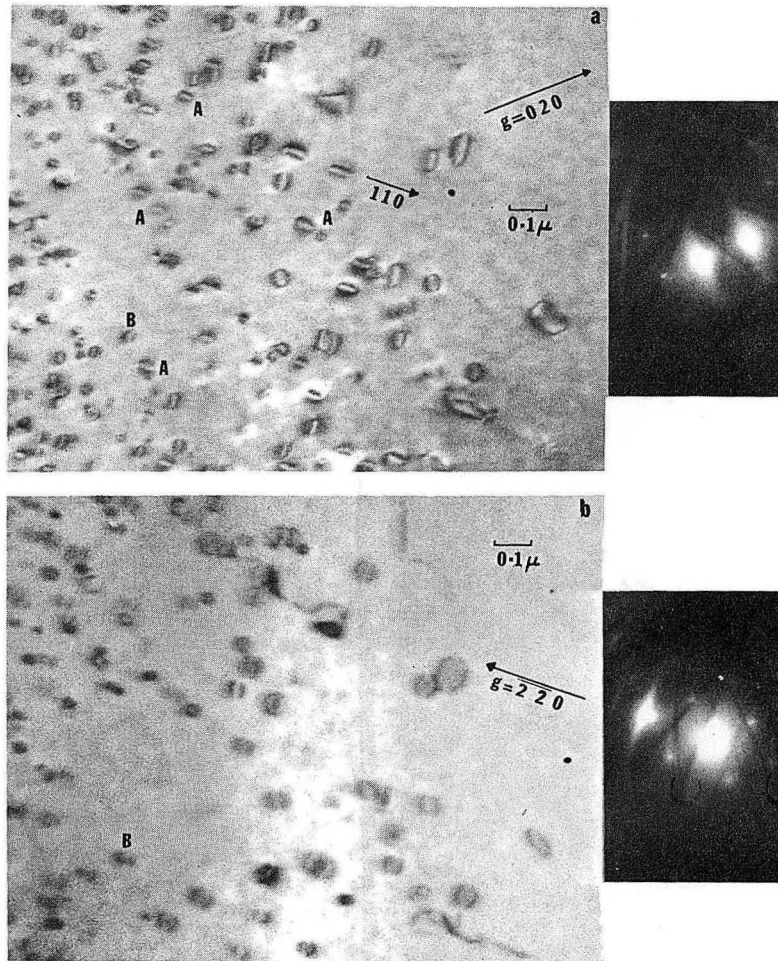
ZN-5105

Fig. 7
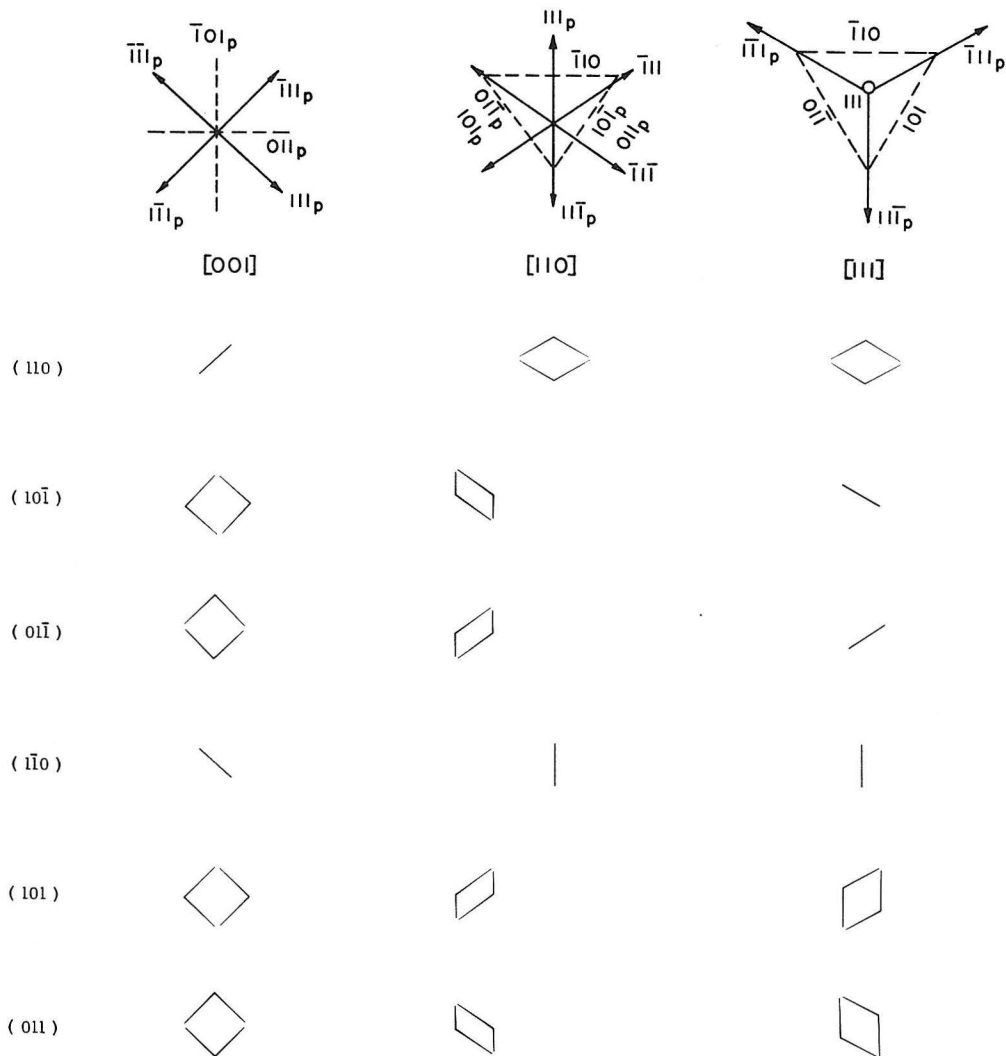
Fig. 8a
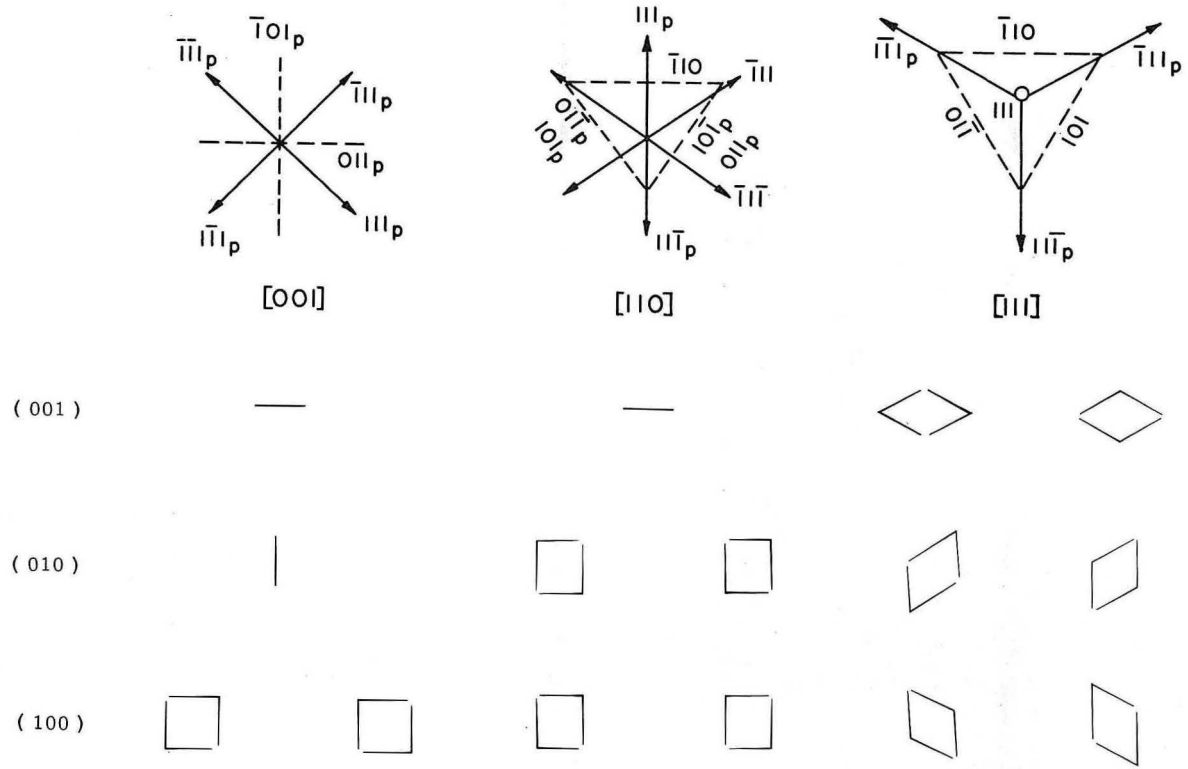
MUB-6949

Fig. 8(b).

MUB-6948
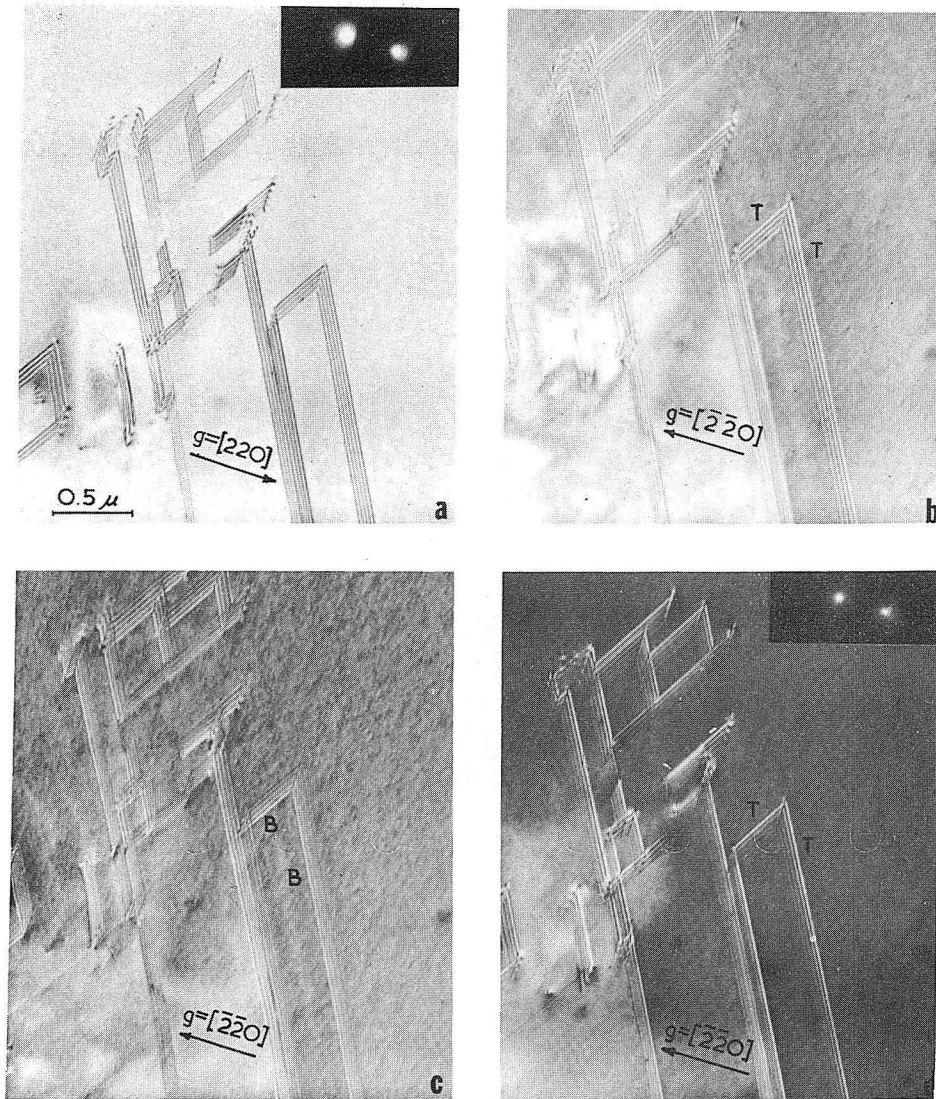
Fig. 9.
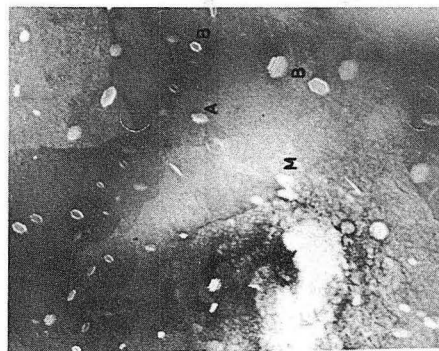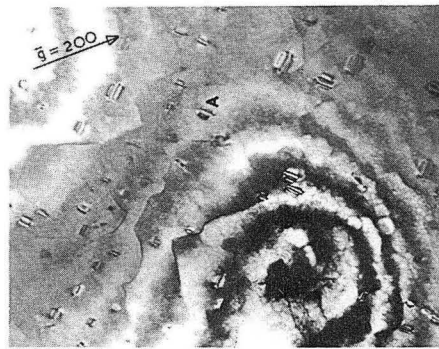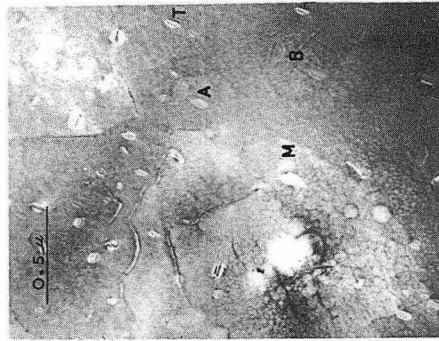
ZN-5197

ZN-5216

Fig. 10.
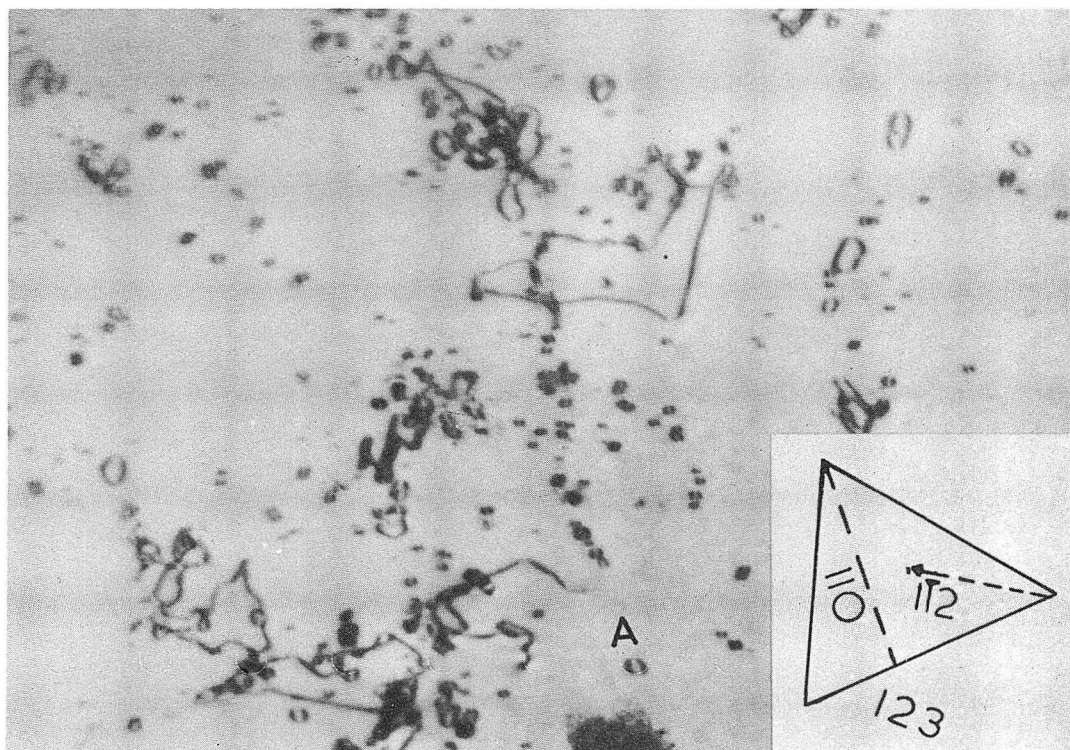
ZN-5212

Fig. 11.

ZN-5214

Fig. 12(a, b).

Fig. 12(c).

$g = [\bar{1}10]$

$= \overline{0.1\mu}$

$1\bar{1}1p$ $\bar{1}\bar{1}1p$ $\bar{1}11p$ $g = \bar{1}10$

$00\bar{1}p$ $010p$ $[112]$
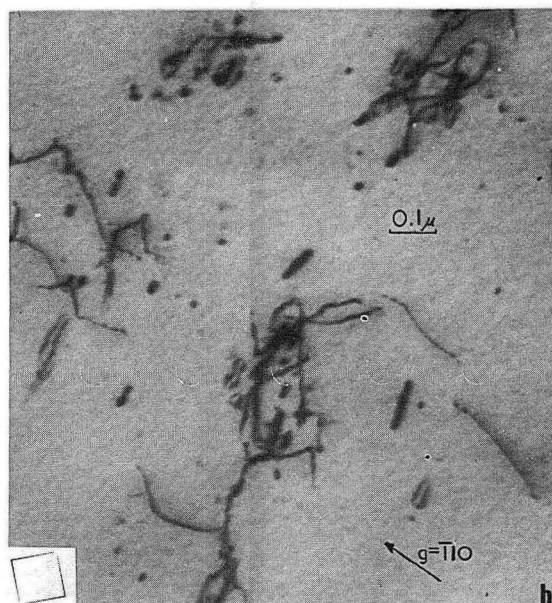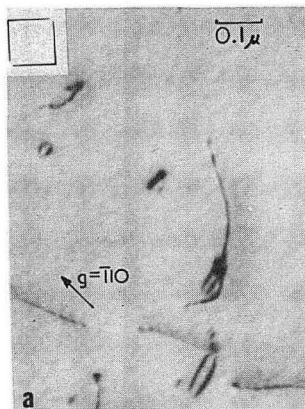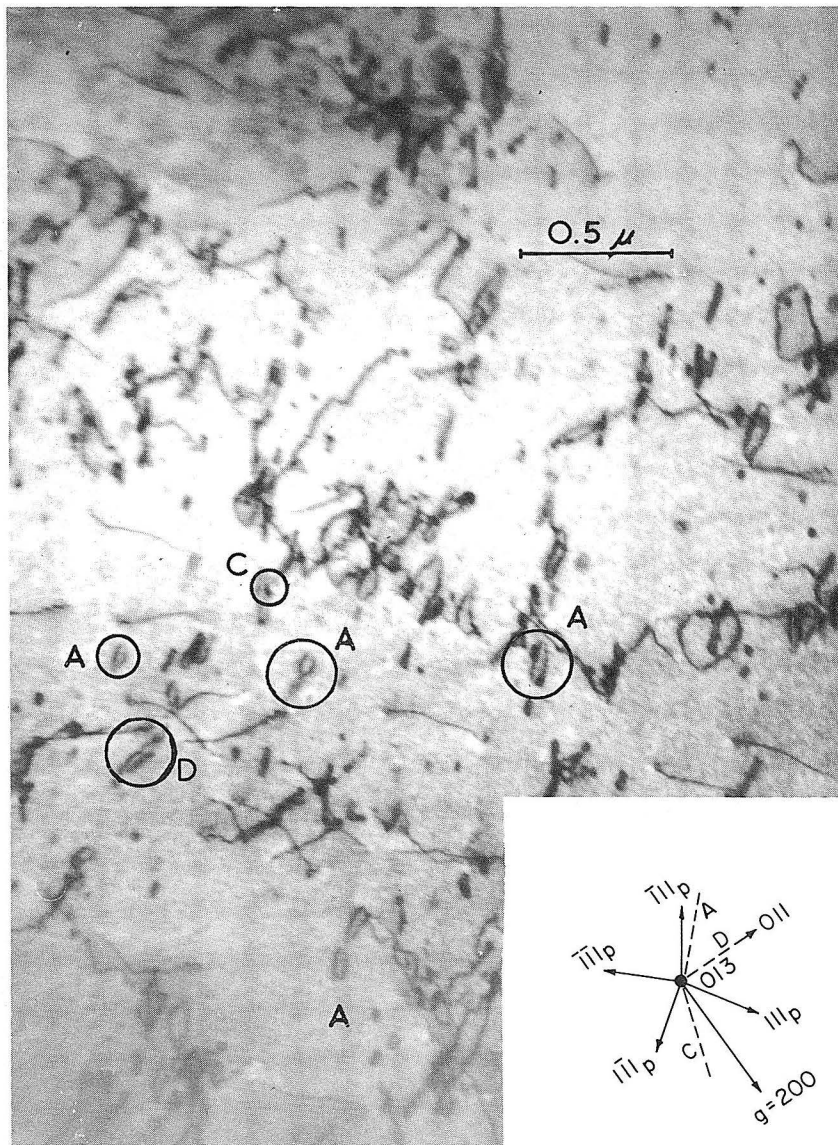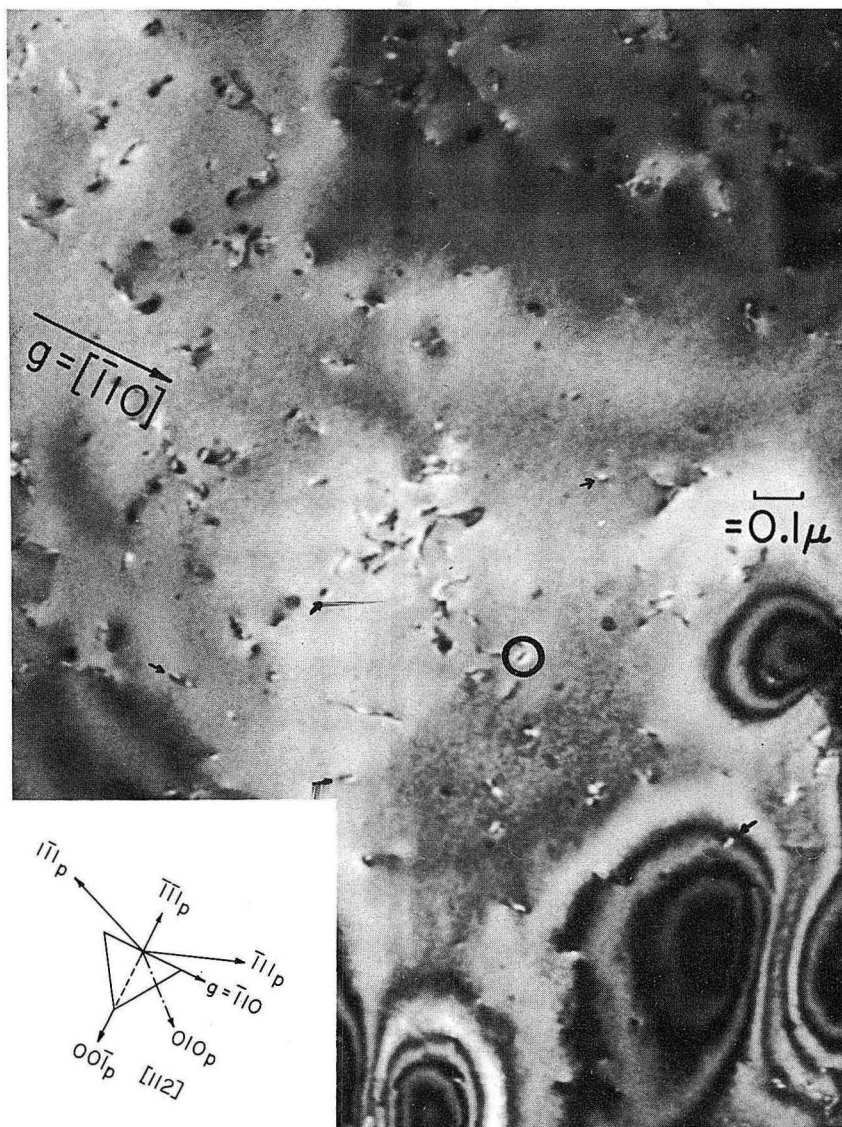
ZN-5060

Fig. 13.
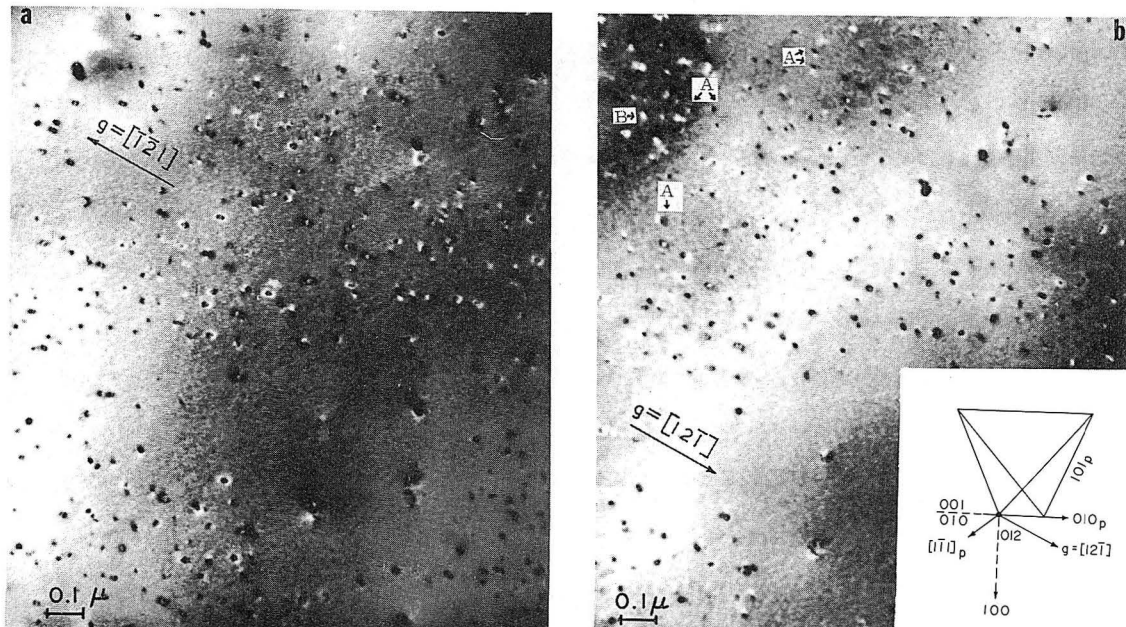
ZN-5063

Fig. 14(a, b).

MU-36192

Fig. 15.

(a) s < 0

(b) s = 0

0.5μ

(c) s > 0

g = [220]
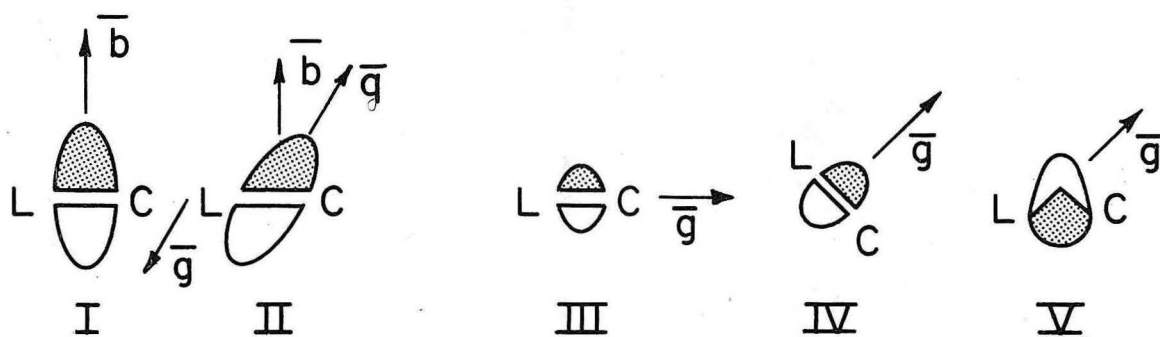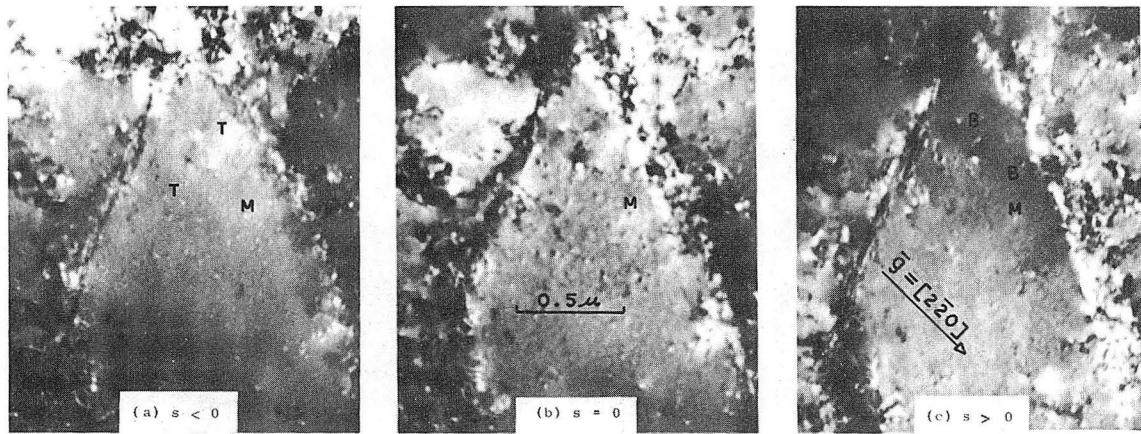
ZN-5199

Fig. 16.

ZN-5217

Fig. 17.

(a)

(b)

ZN-4802

Fig. 18.

g=[111]

g=[1̄1̄1̄]
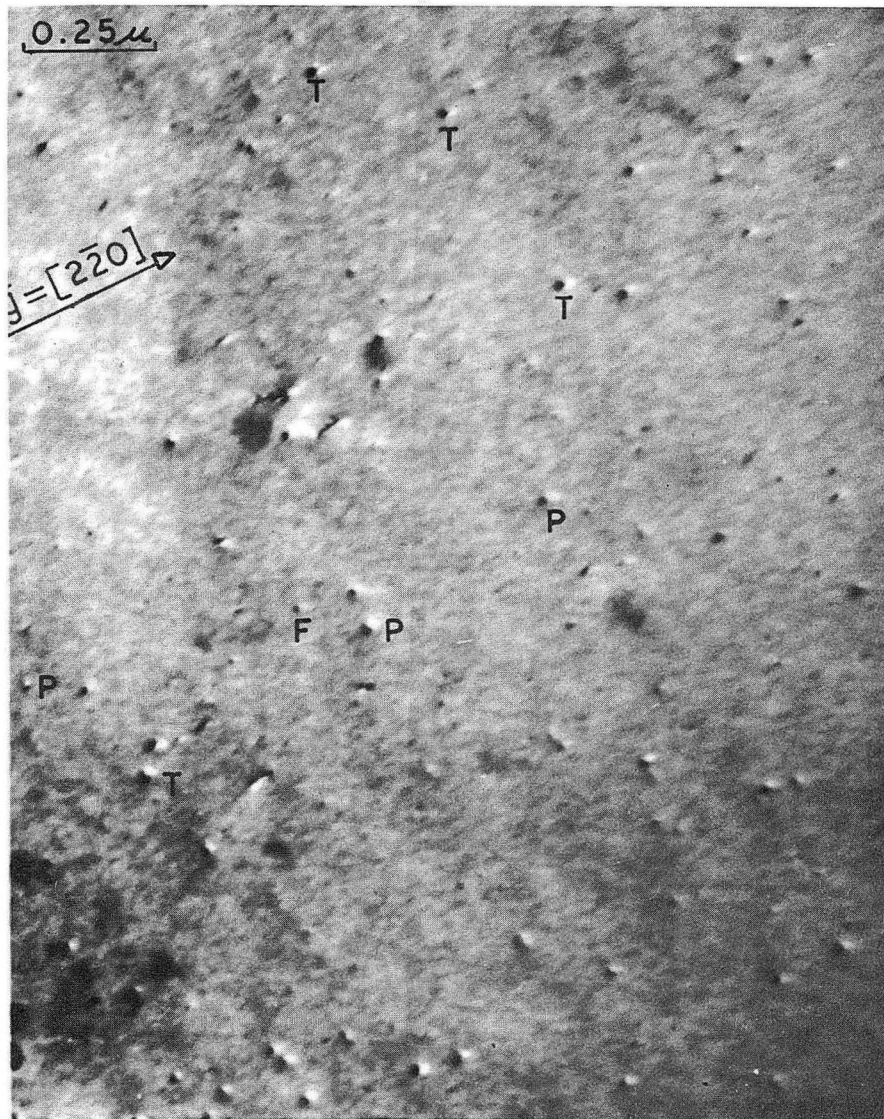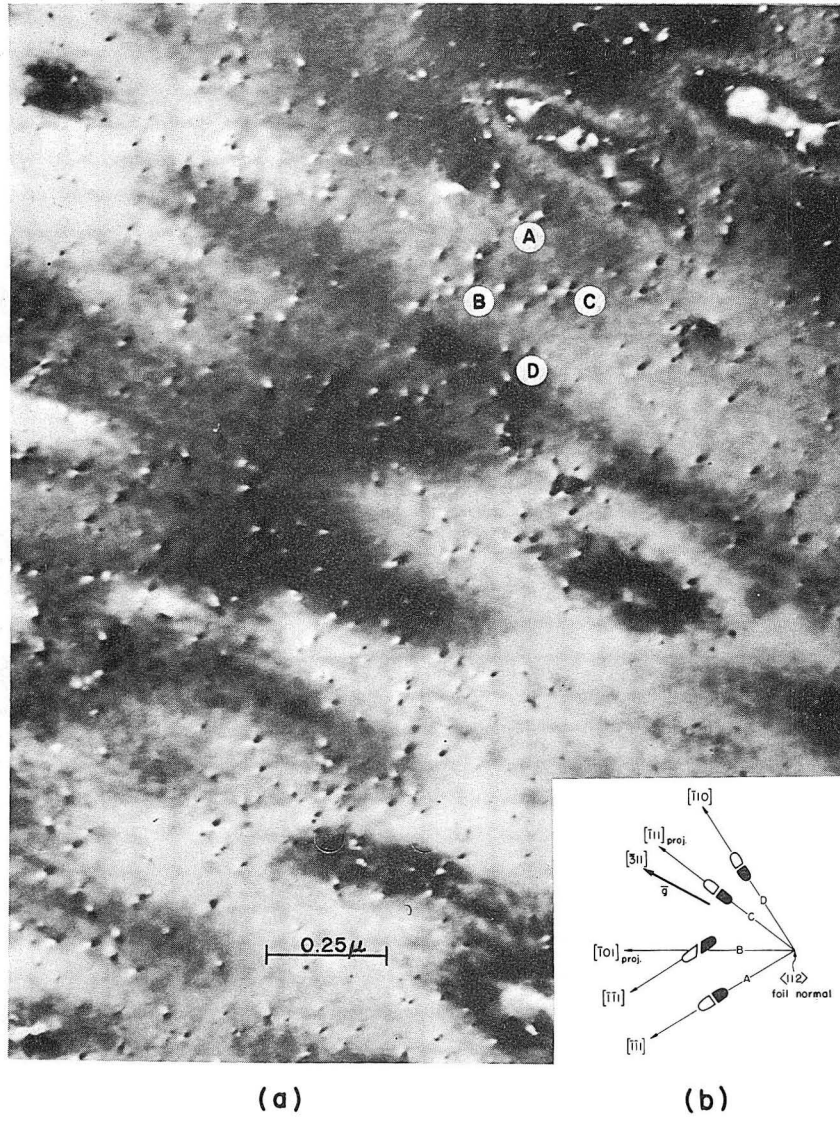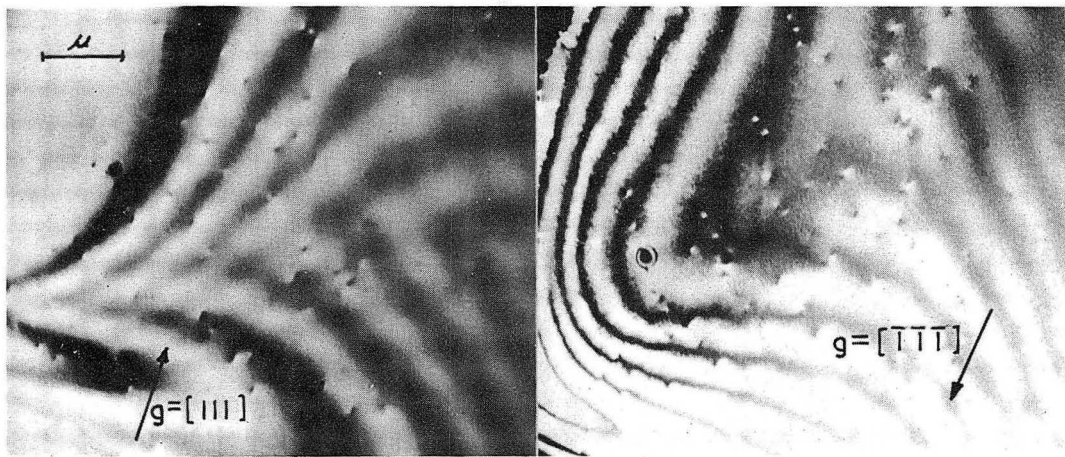
ZN-5211

Fig. 19.

ZN-5215

Fig. 20.

Fig. 21.

ZN-5210